

Astronomy & Astrophysics manuscript no.
(will be inserted by hand later)

The planet search program at the ESO Coudé Echelle spectrometer. *

III. The complete Long Camera survey results.

M. Endl^{1,2,3}, M. Kürster^{3,4}, S. Els^{5,4,3,7}, A. P. Hatzes⁴, W.D. Cochran², K. Dennerl⁶, and S. Döbereiner⁶

¹ Universität Wien, Institut für Astronomie, Türkenschanzstr. 17, A-1180 Wien, Austria

² McDonald Observatory, The University of Texas at Austin, Austin, TX 78712-1083, USA,
e-mail M.Endl: mike@astro.as.utexas.edu, W.D.Cochran: wdc@shiraz.as.utexas.edu

³ European Southern Observatory, Casilla 19001, Vitacura, Santiago 19, Chile

⁴ Thüringer Landessternwarte Tautenburg, Sternwarte 5, 07778 Tautenburg, Germany,
e-mail M.Kürster: martin@tls-tautenburg.de, A.P.Hatzes: artie@jupiter.tls-tautenburg.de

⁵ Isaac Newton Group of Telescopes, Apartado de Correos 321, E-38700 Santa Cruz de La Palma, Spain,
e-mail S.Els: sels@ing.iac.es

⁶ Max-Planck-Institut für extraterrestrische Physik, Giessenbachstr., D-85748 Garching, Germany
e-mail K.Dennerl: kod@mpe.mpg.de

⁷ Universität Heidelberg, Institut für Theoretische Astrophysik, Tiergartenstr. 15, D-69121 Heidelberg, Germany,

Received date / accepted date

Abstract. We present the complete results of the planet search program carried out at the ESO Coudé Echelle Spectrometer (CES) on La Silla, using the Long Camera from Nov. 1992 to April 1998. The CES survey has monitored 37 late-type (F8V – M5V) stars in the southern hemisphere for variations in their differential radial velocities (*RV*) in order to detect Doppler reflex motions caused by planetary companions. This led to the discovery of the first extrasolar planet in an Earth-like orbit around the young (ZAMS) and active G0V star ι Horologii (Kürster et al. 2000). Here we present the *RV* results for all survey stars and perform a statistical examination of the whole data-set. Each star is tested for *RV* variability, *RV* trends (linear and non-linear) and significant periodic signals. β Hyi and ϵ Ind are identified as long-term, low-amplitude *RV* variables. Furthermore, for 30 CES survey stars we determine quantitative upper mass-limits for giant planets based on our long-term *RV* results. We find that the CES Long Camera survey would have detected short-period (“51 Peg-type”) planets around *all* 30 stars but no planets with $m \sin i < 1 M_{\text{Jup}}$ at orbital separations larger than 2 AU. Finally, we demonstrate that the CES planet search can be continued without applying velocity corrections to the *RV* results coming from the currently installed Very Long Camera at the CES.

Key words. Stars: planetary systems – Stars: binaries: spectroscopic – Stars: low-mass, brown dwarfs – Techniques: radial velocities

1. Introduction

The exciting discoveries of giant planets orbiting solar-type stars by precise Doppler searches have caused a shift in our paradigm of the structure and formation of planetary systems. Although we now know that planets have also formed around stars other than the Sun, their orbital characteristics turned out to be quite exotic (for an overview see e.g. Marcy, Cochran & Mayor 2000).

Extrasolar giant planets were detected in very close-by orbits around their host stars with periods on the order of a few days, while orbital eccentricities at longer periods appear to be distributed quite uniformly. To date no Solar System analogue has been detected which is primarily due to the insufficient time baseline and long-term *RV* precision of present Doppler surveys. However, the detection of Jovian-mass companions with $P > 10$ yrs will become possible in the near future.

Send offprint requests to: M. Endl: mike@astro.as.utexas.edu

* Based on observations collected at the European Southern Observatory, La Silla

One of these long-term *RV* surveys is the planet search program at the Coudé Echelle Spectrometer (CES) at ESO La Silla, which was begun in Nov. 1992 using the

1.4 m CAT telescope. The highlight of this program so far was the discovery of an extrasolar giant planet in an Earth-like orbit around the young (ZAMS) and modestly active G0V star ι Horologii (Kürster et al. 2000).

It is important to set such discoveries into the context of the complete results obtained by planet search programs. The pioneering study by Walker et al. (1995) first presented long-term (12 years) RV results for a sample of 21 stars and discussed the implications of their non-detections on the occurrence of Jovian-type planets around solar-type stars. In an even earlier work, Murdoch et al. (1993) presented an analysis of their RV measurements for 29 stars over 2.5 years, finding no brown dwarf companions within 10 AU in their sample. Since then RV measurement precision (e.g. Butler et al. 1996) and the size of target samples has increased dramatically. Extrasolar giant planets, which can be detected by present Doppler searches, exist around $\approx 3 - 5\%$ of the observed solar-type stars. Another study of the long-term RV behaviour of a sample of stars was presented by Cumming et al. (1999). These authors examined 11 years of RV data collected by the Lick survey for 76 F-, G-, and K-type stars and derived companion limits for these stars.

With this work we present all RV measurements of the CES survey and a complete analysis thereof over the time period of November 1992 to April 1998. During that time observations were performed with the same telescope and spectrograph configuration and thus form a homogenous data set. After April 1998 the CES instrument underwent major modifications and the results based on data collected after that point of time will be presented in an upcoming paper.

The structure of this paper is the following: Sect. 2 gives an overview of the CES planet search program, Sect. 3 presents the complete RV results of the CES targets (appendix A displays the RV measurements graphically for each star), Sect. 4 is a statistical examination of the CES RV data where we perform tests to identify variable stars, the presence of linear and non-linear trends and periodic signals, in section 5 we set quantitative upper mass-limits for orbiting planets based on the RV results (appendix B shows the derived limits for each survey star) and finally Sects. 6 and 7 contain the discussion and summary.

2. The Coudé Echelle Spectrometer planet search program on La Silla

The search for extrasolar planets in the southern hemisphere using the Coudé Echelle Spectrometer at ESO La Silla was started in November 1992 (Kürster et al. 1994; Hatzes et al. 1996). At the beginning, the CES survey was a “classical” RV planet search program in the sense that at a time when no extrasolar planet had been found, the common expectation was to discover planets similar to Jupiter. Thus the observing strategy was tailored for long-period and low amplitude signals. Observations were performed on an irregular temporal basis, starting with 2-night runs performed every other month. The sampling

density was later increased, after the discovery of the short-period planet around 51 Peg by Mayor & Queloz (1995), to assure also detection capability for planets of this type.

2.1. The target sample

At the beginning of the survey targets were selected according to the following criteria: Stars with $V < 6$ (with few exceptions) to attain a sufficient S/N-ratio, spectral type F8V - M5V, Stars with declination $< 10^\circ$ to avoid overlap with surveys in the northern hemisphere (again with some exceptions), known (at that time) close binaries were rejected (with the α Centauri system being another exception) and known active stars were neglected.

The final target list consists of 37 bright late-type stars (mostly) in the southern hemisphere: 6 F-, 21 G-, 7 K-, and 3 M-type stars. Table 1 summarizes all targets with their HR, HD and GJ catalogue number, spectral classification, V -magnitudes, distance in parsecs, chromospheric emission indices ($\log R'_{HK}$) and their X-ray luminosity (L_X). Distances are based on the *Hipparcos* parallaxes (ESA (1997)), the $\log R'_{HK}$ -values are taken from the survey of Ca II H & K emission in southern solar-type stars by Henry et al. (1996) and the L_X values are coming from the RASS (ROSAT All Sky Survey) results (Hünsch et al. 1998, 1999). Chromospheric emission in the cores of the Ca II H&K lines and the X-ray luminosities serve as stellar activity indicators since increased chromospheric Ca II H&K and coronal X-ray emission is a common sign of active stars. Stellar activity can produce intrinsic RV variability and adds an additional noise source into the RV measurement (e.g. Saar & Donahue 1997). It can even mimic the RV signature of a short-period planet like in the case of HD 166435 (Queloz et al. 2001). In 1992 the Ca II and X-ray results were not known, which would have probably led to the exclusion of stars like κ For, ι Hor, α For and HR 8883. Fig. 1 and Fig. 2 show the V -magnitude and distance histograms of the CES target sample.

Not all targets were monitored since November 1992: three targets, HR 753, HR 5568 and GJ 433, were added to the sample in May 1997 as *Hipparcos* candidates for having short-period substellar companions (H.-H. Bernstein & U. Bastian priv. comm.), while HR 7373 was only observed for a short time in 1996 and 1997 searching for a short-period planetary companion.

Although listed as a target, τ Cet was mainly included as a reference object since it is a known long-term RV -constant star (Campbell et al. 1988; Walker et al. 1995) and two other stars with known extrasolar planets, 51 Peg (Mayor & Queloz 1995) and 70 Vir (Marcy & Butler 1996), were also observed after 1995 to serve as RV precision check stars.

HR	HD	GJ	Name	Sp.type	V [mag]	d [pc]	$\log R'_{\text{HK}}$	L_X 10^{27} [erg/s]
77	1581	17	ζ Tuc	F9V	4.2	8.59	-4.85	
98	2151	19	β Hyi	G2IV	2.8	7.47	-4.99	6.4
209	4391	1021		G1V	5.8	14.94	-4.55	55.8
370	7570	55	ν Phe	F8V	4.96	15.05	-4.95	14.3
448	9562	59.2		G2IV	5.76	29.66	-5.10	
506	10647	3109		F9V	5.52	17.35		
509	10700	71	τ Cet	G8V	3.5	3.65	-4.96	1.1
695	14802	97	κ For	G0V	5.19	21.93		397.1
753	16160	105A		K3V	5.82	7.21	-4.85	1.8
810	17051	108	ι Hor	G0V	5.41	17.24	-4.65	68.3
963	20010		α For	F8V	3.87	14.11		524.6
1006	20766	136	ζ^1 Ret	G2.5V	5.54	12.12	-4.65	5.8
1010	20807	138	ζ^2 Ret	G1V	5.24	12.08	-4.79	
1084	22049	144	ϵ Eri	K2V	3.73	3.22	-4.47	20.9
1136	23249	150	δ Eri	K0IV	3.51	9.04	-5.22	0.9
2261	43834	231	α Men	G6V	5.1	10.15	-4.94	2.9
2400	46569	1089		F8V	5.58	37.22		
2667	53705	9223A		G3V	5.54	16.25	-4.93	
3259	69830	302		G7.5V	5.95	12.58		3.0
3677	79807			G0III	5.86	192.31		
4523	102365	442A		G3V	4.91	9.24	-4.95	
4979	114613	9432		G3V	4.85	20.48	-5.05	23.0
5459	128620	559A	α Cen A	G2V	-0.01	1.347	-5.00	2.2
5460	128621	559B	α Cen B	K1V	1.33	1.347	-4.92	2.2
5568	131977	570A		K4V	5.74	5.91	-4.48	3.5
6416	156274	666A		G8V	5.47	8.79	-4.94	1.9
6998	172051	722		G4V	5.86	12.98	-4.89	4.3
7373	182572	759		G8IV	5.16	15.15		3.9
7703	191408	783A		K3V	5.31	6.05	-4.99	
7875	196378	794.2	ϕ^2 Pav	F8V	5.12	24.19		
8323	207129	838		G0V	5.58	15.64	-4.80	11.2
8387	209100	845	ϵ Ind	K4.5V	4.69	3.63	-4.56	1.6
8501	211415	853A		G3V	5.33	13.61	-4.86	12.2
8883	220096			G4III	5.66	100.81		34175
		699	Barnard	M4V	9.54	1.82		0.1
		433		M2V	9.79	9.04		
		551	Prox Cen	M5Ve	11.05	1.29		1.7

Table 1. Target list of the CES planet search program. HR, HD and GJ catalogue numbers, spectral type, visual magnitude V , distance in parsec (based on *Hipparcos* parallaxes), chromospheric emission index from Henry et al. (1996) and X-ray luminosity L_X from Hünsch et al. (1998,1999) are given.

2.2. Observations

All stars were observed with the 1.4 m Coudé Auxiliary Telescope (CAT) on La Silla which fed the CES via a direct beam from the telescope. All spectra were taken in a single echelle order centered at a wavelength of 5389 Å. The Long Camera yields a resolving power of $R = 100,000$ and a small spectral range of 48.5 Å. After the installation of the Very Long Camera in April 1998 the resolving power of the CES was raised to $R = 230,000$ but the spectral coverage was even reduced (depending on which CCD was used). The results presented in this work all refer to the Long Camera configuration ($R = 100,000$) prior to this modification, which thus form a homogeneous data set.

In order to assure the necessary high long-term precision for RV measurements all CES spectra are self-calibrated by a superimposed absorption spectrum of molecular iodine (I_2) vapor. This is achieved by passing the starlight through a temperature controlled cell filled with I_2 (see also Kürster et al. 1994).

Typical exposure times of the CES survey were 10 to 15 minutes, and the S/N-ratios of the obtained spectra were in the range of 100 to 250. For the brightest targets exposure times were much shorter (in the order of 10 to 30 seconds), while for the faint M-dwarfs we set a maximum exposure time of 30 minutes, in order to minimize timing uncertainties and subsequent systematic errors in the barycentric velocity correction.

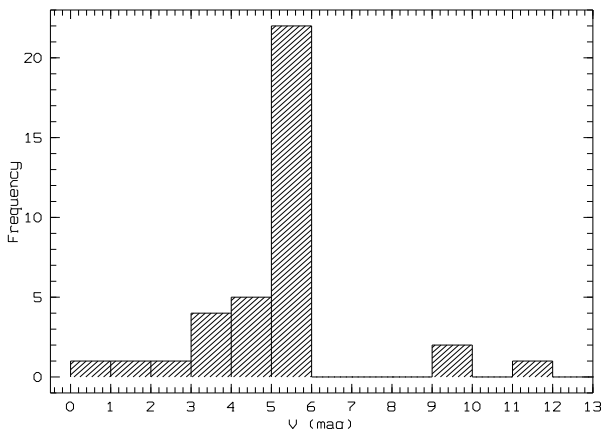


Fig. 1. Histogram of V -magnitudes of the CES targets. The distribution peaks in the magnitude range of 5 - 6 mag while the 3 M-dwarfs form the faint “tail” on the right side.

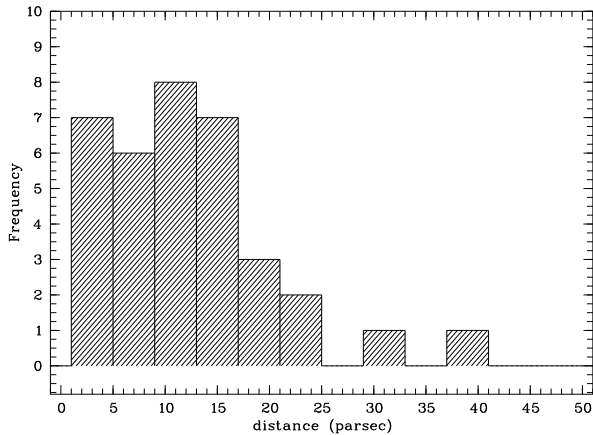


Fig. 2. Histogram of the distances in the CES sample. Not shown are the two stars with distances of more than 100 pc: HR 3677 (192.3 pc) & HR 8883 (100.8 pc). The rest of the targets are located within 50 pc, with the bulk lying closer than 20 pc. Distances are based on *Hipparcos* parallaxes (ESA (1997)).

2.3. Data analysis

To extract the RV information from I_2 self-calibrated spectra it is necessary to perform a full spectral modeling. For the analysis of the CES planet search data we employ the *Austral* code which establishes a model of the observation based on high resolution templates of the stellar and the I_2 spectrum. For a detailed description of this analysis technique we refer the reader to paper I of this series (Endl et al. 2000). The modeling process includes the reconstruction of the shape and asymmetry of the spectrograph instrumental profile (IP) as well as Maximum Entropy Method deconvolution to obtain a higher resolved stellar template spectrum. All computations are carried out on an oversampled sub-pixel grid and a multi-parameter χ^2 -optimization is performed to achieve a best-fit model. The

algorithm follows in general the modeling idea first outlined by Butler et al. (1996) and IP reconstruction techniques by Valenti et al. (1995).

The main limiting factor for the achievable RV precision with the CES is the small spectral bandwidth of 48.5 Å. Using different test scenarios we demonstrated in Endl et al. (2000) that a long-term RV precision of $8 - 15 \text{ m s}^{-1}$ was attained.

3. Radial velocity results

By analysing the complete data set of the CES planet search program until April 1998 with the *Austral* code we obtained precise differential radial velocities for all 37 survey stars. Table 2 summarizes the RV results by giving the total RV rms-scatter, the average internal error for each star, the mean S/N-ratio of the CES spectra and the duration of monitoring by the CES survey. The internal RV measurement error is the uncertainty of the mean value of the RV distribution along one CES spectrum of the typically 90-pixel long spectral segments, for which the modeling is performed independently (see Endl et al. 2000 for a detailed description). A histogram of the RV scatter is shown in Fig. 3, with the exclusion of binaries and the 3 fainter M-dwarfs.

The average RV rms-scatter of the complete target sample (37 stars) is 24.1 m s^{-1} (in the cases of ι Hor (see next section), κ For, HR 2400, HR 3677 (three new binaries, see section 3.2) and α Cen A & B (see Endl et al. 2001a) we take the RV residuals after subtraction of either the planetary or stellar secondary signal). The dependence of the RV scatter on spectral type is demonstrated in Fig. 4. The average RV scatter for F-type stars is 29.8 m s^{-1} (7 stars), for G-type stars 20.7 m s^{-1} (21 stars), for K-type stars 12.3 m s^{-1} (7 stars) and for the M-dwarfs 64.4 m s^{-1} (3 stars). The scatter declines from spectral type F to K, which can be explained as the functional dependence of the measurement precision on the spectral line density (velocity information content) in the CES bandpass. In the case of the short CES spectra the RV precision is clearly depending on the total number of spectral lines within this bandpass. Since the line density is higher for stars with later spectral type, one can expect the highest achievable RV precision for K or M stars. This is the case for K-type stars as demonstrated in Fig. 4. The strong increase of scatter and internal error for the 3 M-type stars is caused by the low S/N-ratio of the obtained spectra (they are all fainter than $V > 9.5$), which degrades the measurement precision despite their higher line density.

Appendix A (Fig. A.1 - Fig. A.10) presents the RV results for all stars, plotted for comparison in the same time frame (JD 2,448,800 to JD 2,451,000). The near sinusoidal RV variation caused by the orbiting planet around ι Hor clearly stands out of the rest of the sample (see Fig. A.3).

For the faint M dwarf Prox Cen ($V = 11.05$) the larger rms-scatter is caused by the insufficient S/N-ratio of the CES spectra obtained with the 1.4 m CAT telescope (the

Star	N	rms [m s ⁻¹]	m.int.err. [m s ⁻¹]	S/N	T [days]
ζ Tuc	51	21.6	16.7	257	1889
β Hyi	157	23.3	20.5	161	1888
HR 209	35	23.1	19.6	151	1573
ν Phe	58	17.9	15.9	212	1927
HR 448	24	17.1	20.5	129	439
HR 506	23	23.9	23.3	173	1574
τ Cet	116	11.3	14.1	196	1889
κ For	40	780.9	14.8	199	1890
HR 753	6	10.1	18.7	118	64
ι Hor	95	52.5	17.4	163	1976
α For	65	55.2	36.8	197	1890
ζ^1 Ret	14	17.7	15.9	109	185
ζ^2 Ret	58	21.8	16.9	180	1977
ϵ Eri	66	13.7	9.7	174	1890
δ Eri	48	15.5	12.9	189	1889
α Men	41	9.8	11.3	170	1853
HR 2400	53	254.9	25.3	150	1925
HR 2667	66	16.5	21.4	144	1935
HR 3259	35	16.2	14.2	124	1852
HR 3677	34	486.1	16.7	145	1925
HR 4523	27	15.0	14.5	210	1925
HR 4979	52	14.0	12.5	185	1934
α Cen A	205	165.3	11.9	225	1853
α Cen B	291	205.1	9.9	206	1853
HR 5568	40	7.7	12.9	114	384
HR 6416	57	25.6	15.0	154	1845
HR 6998	51	19.6	22.9	137	1789
HR 7373	8	8.2	8.9	209	266
HR 7703	30	13.3	14.1	162	1042
ϕ^2 Pav	90	35.4	31.3	184	1969
HR 8323	20	19.8	17.3	147	1068
ϵ Ind	73	13.5	9.9	203	1889
HR 8501	66	34.0	17.5	184	1890
HR 8883	31	65.2	38.6	137	1259
Barnard	24	37.2	46.5	31	1414
GJ 433	15	49.9	61.0	26	337
Prox Cen	65	106.1	88.0	18	1728

Table 2. Radial velocity results of all survey stars. N is the total number of analysed spectra, rms is the total scatter of the RVs, while m.int.err. gives the mean internal measurement error, the mean S/N-ratio of the spectra and T denotes the duration of monitoring (i.e. the timespan from first to last observation of this star).

average S/N-ratio of the Prox Cen spectra is only 18. The results for the inner binary (components A & B) of the α Centauri system were already presented in Endl et al. (2001a). The large scatter seen in the RV results for κ For, HR 2400 and HR 3677 is caused by apparent binary orbital motion and will be discussed in detail.

3.1. The planet orbiting ι Horologii

The G0V star ι Hor (HR 810, $V = 5.4$) has been earlier identified as an RV variable star and thus as a “hot candidate” in the CES survey for having a planetary companion

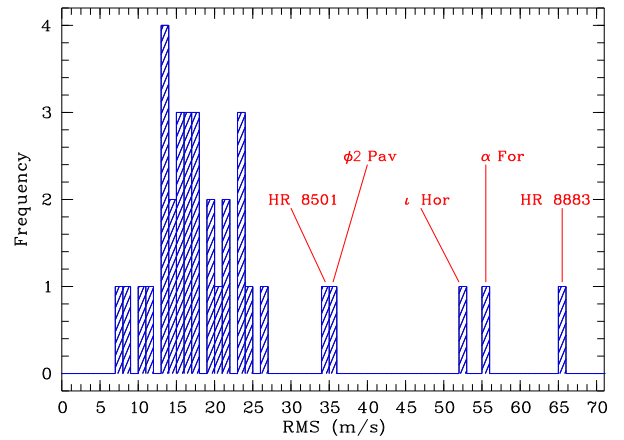


Fig. 3. Histogram of the *RV* scatter of all stars with $\text{rms} < 100 \text{ m s}^{-1}$ and without the 3 faint M-dwarfs. The distribution peaks at 14 m s^{-1} , the stars with higher scatter are: HR 8883 (65.2 m s^{-1}), α For (55.2 m s^{-1}), ι Hor (52.5 m s^{-1}), ϕ^2 Pav (35.3 m s^{-1}) and HR 8501 (34.0 m s^{-1}).

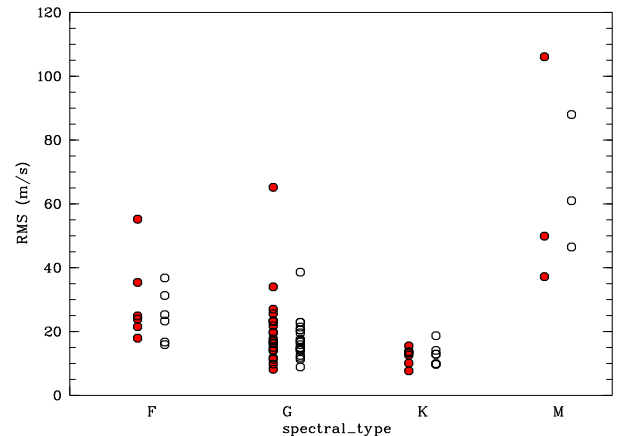


Fig. 4. *RV* scatter (full circles) of the 37 target stars as a function of spectral type. Open circles represent the mean internal measurement error for the stars in each bin. Minimum for both distributions are K-type stars, which can be explained by their higher intrinsic line density, while the increase at faint M-type stars is due to the weak signal.

(Kürster et al. 1998, Kürster et al. 1999a). A possible eccentric Keplerian signal with a period of 600 days was found, but with a low confidence level.

After the analysis of all 95 spectra of ι Hor using the *Austral* code the resulting RVs have a total rms scatter of 52.5 m s^{-1} , an average internal error of 17.4 m s^{-1} and reveal a near sinusoidal variation which is apparent during the last 2 years of monitoring (see Fig. A.3). The 95 spectra were taken between November 1992 and April 1998 and have an average S/N-ratio of 163. A period search within this time series using the Lomb-Scargle periodogram (Lomb 1976, Scargle 1982) detected a highly

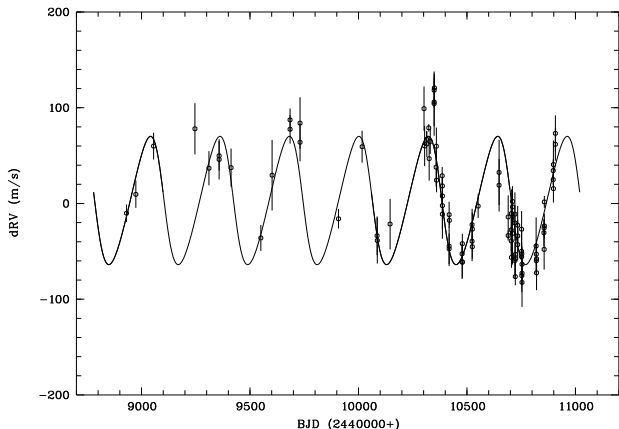


Fig. 5. Keplerian orbital solution for ι Hor (solid line) plotted along the RV data. The RV semi-amplitude K is 67.0 m s^{-1} , the orbital period 320.1 days and the eccentricity $e = 0.16$. The planet has an $m \sin i$ value of $2.26 \text{ M}_{\text{Jup}}$. The residual rms scatter around this best-fit orbit is 27.0 m s^{-1} .

Minimum planet mass	$m \sin i = 2.26 \pm 0.18 \text{ M}_{\text{Jup}}$
Orbital period	$P = 320.1 \pm 2.1 \text{ d}$
Orbital semi-major axis	$a = 0.925 \pm 0.104 \text{ AU}$
Orbital eccentricity	$e = 0.161 \pm 0.069$
RV semi-amplitude	$K = 67.0 \pm 5.1 \text{ m s}^{-1}$
Time of maximum RV	$T_0 = \text{BJD}2,450,306.0 \pm 3.0$
Periastron angle	$\omega = 83^\circ \pm 11^\circ$

Table 3. Parameters of the planet and its orbit around ι Hor.

significant signal with a period of 320 days and a very low False Alarm Probability (FAP) of $< 10^{-11}$. It was possible to find a Keplerian orbital solution for these RV data and thus successfully detect an orbiting extrasolar planet. We presented this discovery already in Kürster et al. (2000) and we refer the reader to this earlier paper for a more detailed description. Here we want to summarize the orbital, planetary and stellar properties. Fig. 5 displays the found Keplerian orbital solution and Table 3 lists the parameters of the planet and its orbit (note that in Kürster et al. 2000 the time of maximum RV was given wrong by one day due to a typo).

ι Hor b was the first planet to be detected residing entirely within the so-called “habitable zone” (as defined in Kasting et al. 1993) of its parent star. The residual rms scatter around the orbit is 27.0 m s^{-1} , larger than the error expected from the RV precision tests in Endl et al. (2000). A lot of this excess scatter is probably caused by stellar activity as it turned out that ι Hor is a quite young (ZAMS) and active star. Both the RV variation caused by the planet as well as the excess scatter have

been confirmed in the meantime by Butler et al. (2001) and Naef et al. (2001).

There are indications that the ι Hor system might host additional planetary companions: the periodogram of the RV residuals (after subtraction of the orbit) reveals a peak at $P \approx 620$ days. This looks intriguing especially after the detections of extrasolar planets moving in near-resonance orbits, e.g. the two companions of HD 83443 in a $10 : 1$ resonance (Mayor et al. 2000), the planetary pair around GJ 876 in a $2 : 1$ resonance (Marcy et al. 2001), and the two planets orbiting 47 UMa in a $5 : 2$ resonance (Fischer et al. 2001). We demonstrate in Kürster et al. (2000) that the $P \approx 620$ days peak is not due to spectral leakage from the $P = 320$ days signal (see panel (d) of Fig. 1 in Kürster et al. 2000). This could indicate the presence of a second planet located close to the $2 : 1$ resonance. However, the FAP of this peak is still above 0.1% and we cannot confirm yet the presence of a second companion. After the replacement of the Long Camera at the CES with the Very Long Camera we continued to monitor ι Hor using the same I_2 -cell for self-calibration. The analysis of the new data and merging it with the Long Camera data set might allow us in the near future to verify the existence of the second planet.

The CES Long Camera results also contributed to another extrasolar planet detection: our RV data for the nearby (3.22 pc) K2V star ϵ Eri add to the evidence for a long-period ($P \approx 6.9$ yrs) planet, as presented in Hatzes et al. (2000).

3.2. Three new spectroscopic binaries: κ For, HR 2400, and HR 3677

κ For, HR 2400 and HR 3677 were found to be single-lined spectroscopic binaries, their large RV scatter (see Table 2) is the direct result of huge RV trends induced by high mass (stellar) companions. These trends were already discovered by an earlier analysis of a fraction of the data of these 3 stars (Hatzes et al. 1996). Now the analysis of the entire Long Camera data of κ For and HR 3677 exhibits a curved shape of the RV trends and - in the case of κ For - allows us to find a preliminary Keplerian orbital solution, while the very long period for HR 3677 and the linearity of the RV trend for HR 2400 prohibits this.

The G0V star κ For has the largest RV scatter ($\text{rms}=780.9 \text{ m s}^{-1}$) of all stars in the CES sample. We find a preliminary Keplerian orbital solution (see Fig. 6) with the following parameters: orbital period $P = 7700$ days, time of periastron passage $T = 2454466 \text{ JD}$, a low eccentricity $e = 0.0576$, an RV semi-amplitude $K = 2302 \text{ m s}^{-1}$ and periastron angle $\omega = 269.07^\circ$. This fit to the 40 RV measurements gives a $\chi^2_{\text{best}} = 38.3$, and a reduced $\chi^2_{\text{red}} = 1.13$ (with 34 degrees of freedom) and $P_\chi(\chi^2) = 0.28$. In other words the found preliminary Keplerian orbit represents a good fit to the RV data. By changing the value of P (and letting the remaining orbital parameters vary until $\chi^2 = \chi^2_{\text{best}} + 1$) we determined the uncertainty of the

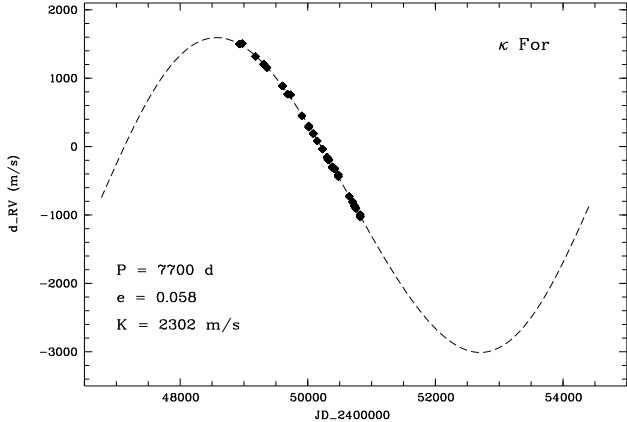


Fig. 6. Preliminary Keplerian orbital solution for κ For, the best-fit orbit (dashed line, $\chi^2_{\text{best}} = 38.3$, $\chi^2_{\text{red}} = 1.13$) is plotted along with the 40 RV measurements (diamonds).

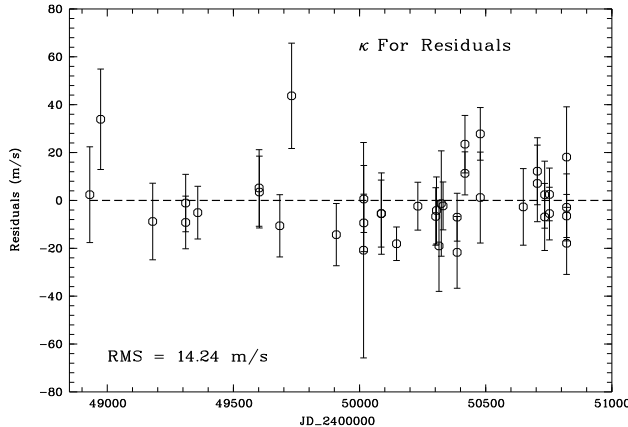


Fig. 7. Residual RV scatter of κ For after subtraction of the best-fit Keplerian orbit (Fig. 6). The rms scatter of 14.24 m s^{-1} agrees well with the mean internal error of 14.8 m s^{-1} .

period to be ± 295 days. Since our RV data cover only a fraction of one orbital cycle and do not constrain the orbit well enough, it was not possible to find a simultaneous solution for all orbital parameters and derive the error-range for the remaining 5 parameters. The mass function is $f(m) = (9.67 \pm 3.17) \times 10^{-3} M_{\odot}$ and the orbital period transforms to $a \approx 8.5$ AU. The scatter around this orbit is 14.24 m s^{-1} (Fig. 7) and consistent with the mean internal error of 14.8 m s^{-1} . In the *Hipparcos* catalogue κ For was given a double/multiple systems annex flag G, meaning that higher-order terms were necessary to find an adequate astrometric solution. This is an indication that κ For is a long-term ($P > 10$ yrs) astrometric binary, consistent with our results. The RV variability of κ For was also noted by Nidever et al. (2002) who find a linear RV slope of -1.73 m s^{-1} per day for their 7 measurements of this star.

HR 2400 (F8V) reveals a linear trend in its RV data indicating a high mass companion in a long-period or-

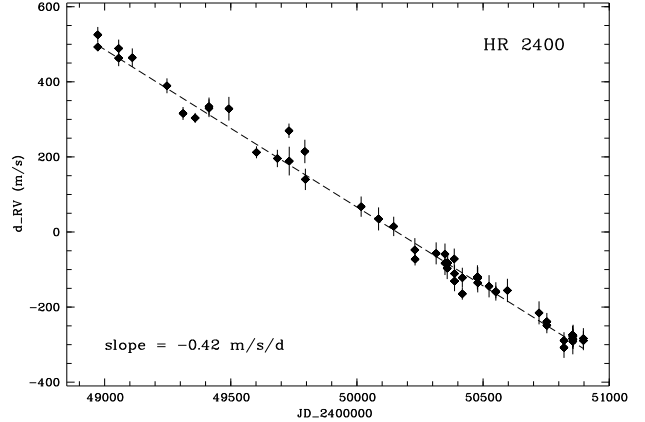


Fig. 8. Linear fit (dashed line) to the RV data of HR 2400 (diamonds with errorbars), the residuals are shown in Fig. 9. This best fit linear trend has a slope of $-0.42 \pm 0.005 \text{ m s}^{-1} \text{d}^{-1}$.

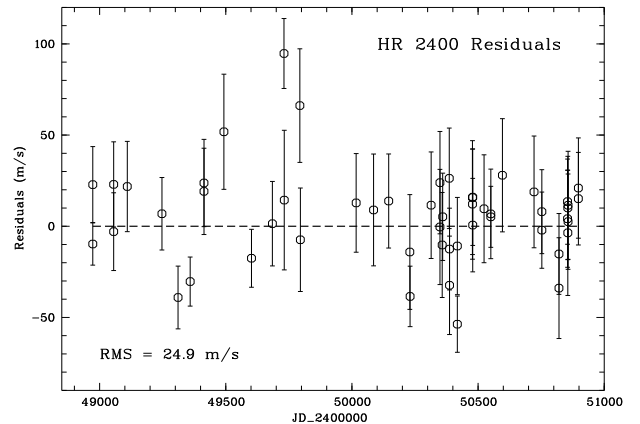


Fig. 9. RV residuals of HR 2400 after subtraction of the linear slope (Fig. 8). The residual rms scatter of 24.9 m s^{-1} is consistent with the mean internal error of 25.3 m s^{-1} .

bit which does not allow us to find a Keplerian orbital solution. Fig. 8 shows the best-fit linear function with a slope of $-0.42 \pm 0.005 \text{ m s}^{-1} \text{d}^{-1}$ (the error range of the slope is determined by varying the value of the slope, whereby for each slope the zero-point is always fitted, until $\chi^2 = \chi^2_{\text{best}} + 1$). The residual rms-scatter around this slope is 24.9 m s^{-1} which is of the same order as the average internal error of 25.3 m s^{-1} (see Fig. 9). The linearity of the trend does not allow an estimate of the mass or period of the secondary. Moreover, HR 2400 does not possess a double/multiple systems annex flag in the *Hipparcos* catalogue indicating that the period is indeed very long compared to the monitoring time spans of both programs (*Hipparcos* : 3.2 yrs, CES Long Camera: 5.2 yrs).

The giant HR 3677 (G0III) is - with a distance of 192.31 pc - by far the most distant star in the CES sample. A parabolic fit to the RV results is shown in Fig. 10. This fit gives an acceptable description of the data with a χ^2_{red} of 0.99 and $P_{\chi}(\chi^2) = 0.48$. Fig. 11 shows the residuals af-

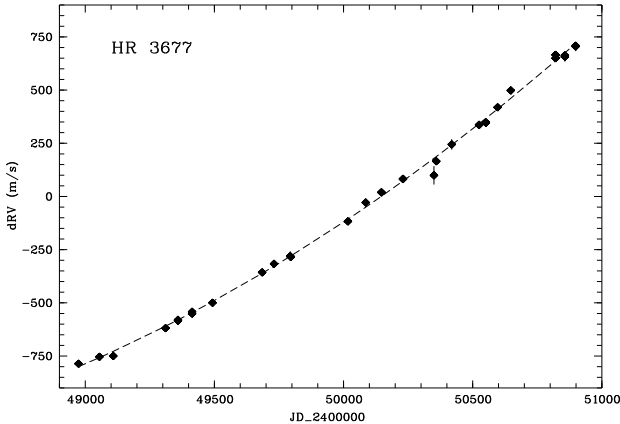


Fig. 10. Best parabolic fit for HR 3677 (G0III) indicating an orbital period much longer than the monitoring time (*Hipparcos* astrometry gives a period of ≈ 75 years). The best-fit curved trend is plotted as dashed line along with our *RV* data (diamonds). The χ^2_{red} of this fit is 0.99, indicating a good fit. See Fig. 11 for the residuals.

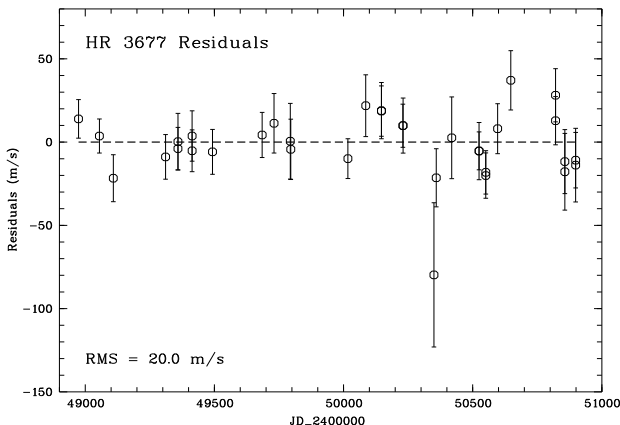


Fig. 11. Residual *RV*s of HR 3677 after subtraction of the best-fit curved trend (shown in Fig. 10). The rms-scatter is 20.0 m s^{-1} slightly larger than the mean internal error of 16.7 m s^{-1} . This larger residual scatter is primarily caused by the one outlier at JD 2,450,350; without this data-point the scatter is reduced to 14.7 m s^{-1} and is consistent with our measurement errors.

ter subtraction of this best-fit curved trend. The residual rms-scatter around this orbit is 20.0 m s^{-1} , slightly larger than the average internal error of 16.7 m s^{-1} . From the *Hipparcos* measurements of HR 3677 a two-component astrometric solution was derived. The angular separation of the components is given as 0.131 ± 0.010 arcseconds which corresponds at the distance of 192.31 pc to a minimum orbital separation of $\approx 25 \pm 2$ AU. The orbital period would be around 75 years, too long to determine a Keplerian solution, but it seems to be consistent with the *RV*-variation we find for HR 3677.

4. Statistical analysis

In the following section we perform a thorough statistical examination of the complete *RV* data set of the CES Long Camera survey. We test each star for variability, linear and curved *RV* slopes and significant periodic signals.

4.1. Probing for variability

To test if a star in the sample is variable we first apply the *F*-test ($F = \sigma_1^2/\sigma_2^2$). We start by comparing the total variance of the *RV* results of one star (σ_1^2) with the rest of the sample ($P(F)_1$ in Table 4). Since, for the small CES bandwidth, the *RV* precision and hence the scatter is a function of spectral type, we compare the stars with the mean scatter (σ_2^2) of the remaining stars within the same spectral type bin (as described in Sect. 3).

For a second *F*-test, we take as the σ_2^2 the individual mean internal *RV* error and determine the $P(F)$ ($P(F)_2$ in Table 4). With this we test if the star is more variable (or more constant) than its internal *RV* error would suggest.

Finally, we fit a constant to the *RV* results (with the zero-point as free parameter) and use the χ^2 -statistic to check whether the constant model delivers a good description of the data. Again a small value of $P_\chi(\chi^2)$ means that the *RV* results for a star have a larger scatter than expected from their internal errors, which then can be interpreted as a sign for variability.

For the binaries (κ For, HR 2400, HR 3677, α Cen A & B) the *RV* residuals after subtraction of either the known binary orbit (α Cen A & B) or the preliminary orbit we have found are taken for the variability tests. For α Cen A & B with the known binary orbit, HR 2400 with its linear trend and HR 3677 with its curved trend, ν the degrees of freedom equals $N - 1$ (the velocity zero-point is adjusted), so that the *F*-test results for these stars are strictly valid only under the assumption that the binary orbit and the velocity trends are precisely known. In the cases of κ For and ι Hor we take $\nu = N - 6$.

As criterion for a significant result we adopt the 99%-level (i.e. $P < 0.01$). Table 4 summarizes the results of these variability tests for all survey stars.

For 5 stars in the CES sample all 3 tests yielded $P < 0.01$ and are thus clearly identified as *RV* variables: ι Hor (residuals), α For, HR 6416, HR 8501 and HR 8883. For ι Hor the cause of the residual variability was already discussed (stellar activity and possible second planet), while in the cases of α For ($L_X = 525 \times 10^{27} \text{ erg/s}$) and HR 8883 ($L_X = 34175 \times 10^{27} \text{ erg/s}$) also a high level of stellar activity appears to be responsible for the detected variability. We found strong Ca II H&K emission for HR 8883 by taking a spectrum with the FEROS instrument and the 1.5 m telescope on La Silla. We will show later that we can also determine the cause of variability for HR 6416 and HR 8501 (we will examine the presence of linear and curved trends in the *RV* data). The case of α For will be further discussed in more detail.

Star	$P(F)_1$	$P(F)_2$	χ^2_{red}	$P_\chi(\chi^2)$
ζ Tuc	0.023	0.073	1.92	0.0001
β Hyi	0.13	0.12	1.51	3.5E-05
HR 209	0.5	0.35	0.98	0.50
ν Phe	3.6E-05	0.367	1.17	0.18
HR 448	0.34	0.40	0.70	0.85
HR 506	0.23	0.90	2.02	0.003
τ Cet	6.6E-11	0.016	0.73	0.98
κ For _{Res}	0.03	0.83	1.09	0.33
HR 753	0.63	0.203	0.32	0.90
ι Hor _{Res}	0.009	4.9E-19	4.8	5.6E-45
α For	1.E-09	0.0014	1.82	6.9E-05
ζ^1 Ret	0.57	0.71	1.55	0.09
ζ^2 Ret	0.67	0.05	1.69	0.0009
ϵ Eri	0.32	0.0059	1.86	3.5E-05
δ Eri	0.06	0.22	1.16	0.21
α Men	3.5E-06	0.37	0.90	0.64
HR 2400 _{Res}	0.13	0.91	1.51	0.012
HR 2667	0.06	0.04	0.68	0.67
HR 3259	0.14	0.45	2.2	7.2E-05
HR 3677 _{Res}	0.87	0.32	0.94	0.57
HR 4523	0.09	0.85	1.57	0.03
HR 4979	0.004	0.41	1.18	0.18
α Cen A _{Res}	0.0001	0.78	0.70	0.94
α Cen B _{Res}	0.88	0.13	1.26	0.12
HR 5568	0.001	0.002	0.38	0.99
HR 6416	0.09	0.0001	3.63	1.4E-18
HR 6998	0.70	0.28	0.55	0.99
HR 7373	0.02	0.83	0.77	0.62
HR 7703	0.65	0.75	0.81	0.76
ϕ^2 Pav	0.05	0.25	1.59	0.0003
HR 8323	0.85	0.56	1.02	0.43
ϵ Ind	0.39	0.0094	1.73	0.0001
HR 8501	3.1E-05	2.7E-07	2.26	3.7E-08
HR 8883	6.8E-10	0.005	4.21	9.3E-14
Barnard	0.0007	0.29	0.57	0.95
GJ 433	0.19	0.46	0.80	0.68
Prox Cen	2.2E-11	0.14	1.61	0.001

Table 4. F-test and χ^2 -test results for the complete sample. $P(F)_1$ is the result of the F-test comparing the RV scatter with the average scatter within a spectral type bin, while $P(F)_2$ gives the results of the comparison with the mean internal RV error. χ^2_{red} is the best (reduced) χ^2 -value after fitting a constant to the RV data and $P_\chi(\chi^2)$ the corresponding probability.

For 17 stars (HR 209, HR 448, κ For, HR 753, ζ^1 Ret, δ Eri, HR 2400 (residuals), HR 2667, HR 3677 (residuals), HR 4523, HR 4979, α Cen B (residuals), HR 6998, HR 7373, HR 7703, HR 8323 and GJ 433) all 3 tests resulted in $P > 0.01$ and thus no sign of variability whatsoever can be found for these stars. 5 stars are less variable than the rest of the sample (which of course also results in a low $P(F)_1$): ν Phe, τ Cet, α Cen A (residuals), HR 5568 and Barnard's star.

ϵ Eri and ϵ Ind both have a $P(F)_1 > 0.01$ (i.e. their overall RV scatter is quite typical for the CES sample)

but a low $P(F)_2$ and $P_\chi(\chi^2)$, making them candidates for low-amplitude variations.

ζ Tuc, β Hyi, HR 506, ζ^2 Ret and ϕ^2 Pav all appear unsuspicious in both F-tests but their RV data is not well fit by a constant function. Maybe an inclined linear or curved trend will describe these RV data better.

Finally, Prox Cen is more variable than the rest of the CES M-dwarf sample (of same spectral type) but not if compared to its own intrinsic mean RV error, however, for this star the $P_\chi(\chi^2)$ for a constant fit is still less than 0.01.

4.2. RV trends: linear and curved slopes

As the next step in the statistical analysis we examine whether the RV data of those stars which showed up as variable by the previous tests can be better described by a linear slope or a curved trend. For this purpose we determine the best-fit linear and parabolic function by χ^2 -minimization and again compute $P_\chi(\chi^2)$ for the following 12 stars: ζ Tuc, β Hyi, HR 506, α For, ζ^2 Ret, ϵ Eri, HR 6416, ϕ^2 Pav, HR 8501, HR 8883, ϵ Ind and Prox Cen.

Table 5 shows the results of the slope and curvature tests. For 7 stars of the sample (ζ Tuc, HR 506, ζ^2 Ret, ϵ Eri, ϕ^2 Pav, HR 8883, Prox Cen) the resulting probabilities $P_\chi(\chi^2)$ remain below 0.01. For these stars no linear or curved trend delivers a satisfactory explanation for their RV variations.

For ϵ Eri the $P_\chi(\chi^2)$ -value for a curved trend is a magnitude higher than for a linear trend. As described in detail in Hatzes et al. (2000) there is evidence for a long-period ($P \approx 2500$ days), low amplitude ($K \approx 19 \text{ m s}^{-1}$) planet orbiting ϵ Eri. The difference we find between the linear and curved trend fits (see Fig. 12) might indicate the presence of the RV signature of this planet. The rms-scatter around the curved trend is with 12.9 m s^{-1} still larger than the mean internal error of 9.7 m s^{-1} , which is not surprising for the modestly active star ϵ Eri.

For 5 stars (β Hyi, α For, HR 6416, ϵ Ind and HR 8501) the linear slope tests resulted in a significant increase in $P_\chi(\chi^2)$. This is a true indication for the presence of a linear trend in their RV behavior. However, for none of them, the probability of a curved trend is found to be significantly higher than for a linear one, except for β Hyi where the difference is 5%. Table 6 gives the values of RV shift per day of the found linear trends and the remaining RV scatter around those trends. With the exception of α For the RV trends are all positive, with HR 8501 having the strongest slope of $+0.057 \text{ m s}^{-1} \text{d}^{-1}$ and ϵ Ind with the smallest variation of $+0.011 \text{ m s}^{-1} \text{d}^{-1}$. Fig. 13 to 17 display the best-fit trends in the RV results for these 5 stars.

Since HR 6416 and HR 8501 are known binary stars, the detected linear RV trend can be attributed to the binary orbital motion. The *Hipparcos* catalogue gives an angular separation of 8.658 arcseconds for the HR 6416

Star	$P_\chi(\chi^2)_{\text{constant}}$	$P_\chi(\chi^2)_{\text{linear}}$	χ^2_{red}	$P_\chi(\chi^2)_{\text{curvature}}$	χ^2_{red}
ζ Tuc	0.0001	0.0001	1.93	7.6E-05	1.96
β Hyi	3.5E-05	0.19	1.10	0.24	1.07
HR 506	0.003	0.005	1.98	0.003	2.07
α For	6.9E-05	0.03	1.36	0.025	1.38
ζ^2 Ret	0.0009	0.001	1.67	0.001	1.69
ϵ Eri	3.5E-05	3.3E-05	1.86	0.0005	1.70
HR 6416	1.4E-18	0.056	1.32	0.059	1.32
ϕ^2 Pav	0.0003	0.0004	1.59	0.0003	1.60
ϵ Ind	0.0001	0.035	1.33	0.038	1.32
HR 8501	3.7E-08	0.86	0.81	0.93	0.75
HR 8883	9.3E-14	1.5E-13	4.32	9.3E-14	4.37
Prox Cen	0.001	0.002	1.59	0.0025	1.59

Table 5. Results of linear slope and curvature tests. Probabilities $P_\chi(\chi^2)$ and χ^2_{red} -values are given for the best-fit linear and parabolic functions. The first column ($P_\chi(\chi^2)_{\text{constant}}$) is repeated from Table 4 for comparison purposes.

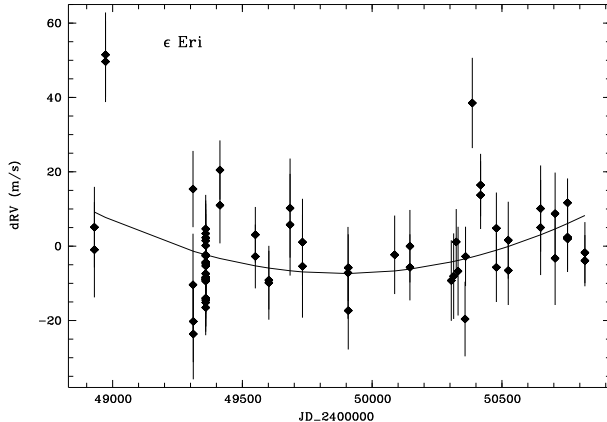


Fig. 12. Best-fit curved RV trend for ϵ Eri. With $\chi^2_{\text{red}} = 1.7$ and $P_\chi(\chi^2)_{\text{curv}} = 0.0005$ this fit is still a poor description of the RV results. However, $P_\chi(\chi^2)_{\text{curv}}$ is a magnitude higher than for a linear fit. The presence of the highly eccentric Keplerian signal of the planet described in Hatzes et al. (2000) is already indicated here.

binary. At a distance of 8.79 pc this implies a minimum separation of 76.1 AU. In the Gliese catalogue of nearby stars HR 6416 is listed as GJ 666A and the secondary GJ 666B as an M0V dwarf. We adopt $0.89 M_\odot$ as mass value for the G8V primary and for the secondary $0.52 M_\odot$ (after Gray 1988). Assuming a circular orbit and the minimum separation as the true separation and using Kepler's third law we can find an estimate for the RV acceleration for HR 6416. The orbital period is ≈ 565 yrs and the RV semi-amplitude $K \approx 1442 \text{ m s}^{-1}$. Since the observing time span is not even a 1/100 of one orbital cycle we linearly interpolate to find an *average* acceleration of $\approx 0.028 \text{ m s}^{-1} \text{d}^{-1}$ which is in good agreement with the detected trend of $0.032 \pm 0.003 \text{ m s}^{-1} \text{d}^{-1}$.

The angular separation for the HR 8501 binary (GJ 853A & B) is given by the Gliese catalogue as 3.4 arcseconds. This transforms into a minimum orbital separa-

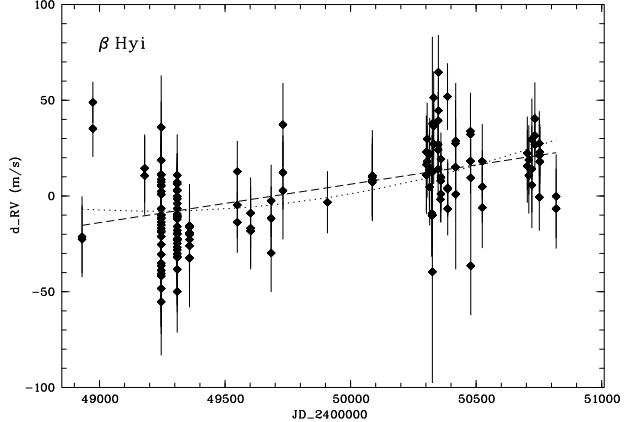


Fig. 13. β Hyi RV data and the best-fit linear slope (dashed line) and curved trend (dotted line). The rms scatter around these trends is 19.3 m s^{-1} and 19.5 m s^{-1} respectively. The found linear trend is $+0.02 \pm 0.0024 \text{ m s}^{-1} \text{d}^{-1}$.

tion of 46.3 AU at the distance of 13.61 pc. The spectral type of the secondary (GJ 853B) is unknown and therefore no mass estimate is possible. Assuming an M0V companion the average linear RV trend for the G3V primary ($1.04 M_\odot$) would be $\approx 0.075 \text{ m s}^{-1} \text{d}^{-1}$, slightly larger than the found trend of $+0.057 \pm 0.006 \text{ m s}^{-1} \text{d}^{-1}$. The difference can easily be explained either by a larger orbital separation than the projected minimum value, the $\sin i$ -effect, a lower mass of the secondary, the orbital phase corresponds to a steeper part of the RV -curve, or a combination of all these effects.

α For is also a known binary with an angular separation of 4.461 arcseconds (from *Hipparcos* catalogue). At a distance of 14.11 pc this means $a \approx 63$ AU. Adopting a mass for the F8V primary of $1.2 M_\odot$ (after Gray 1988) and assuming again an M0V secondary (the spectral type of the companion is unknown) we find an average acceleration of $0.04 \text{ m s}^{-1} \text{d}^{-1}$ which is exactly the value of the RV trend we observe for α For. However, the rms scat-

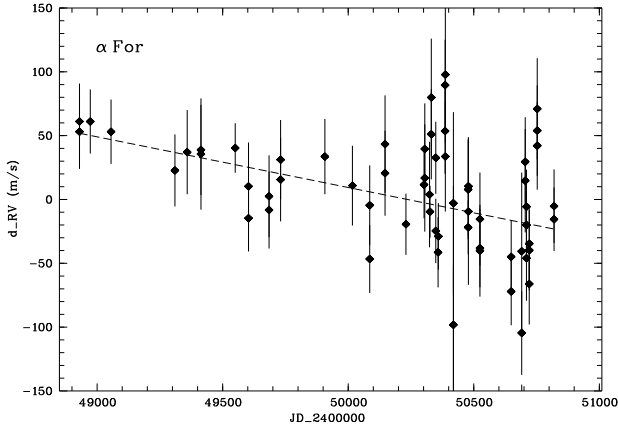


Fig. 14. Linear trend in the *RVs* of α For. The slope of $-0.04 \pm 0.007 \text{ ms}^{-1}\text{d}^{-1}$ has a residual scatter of 50.9 ms^{-1} .

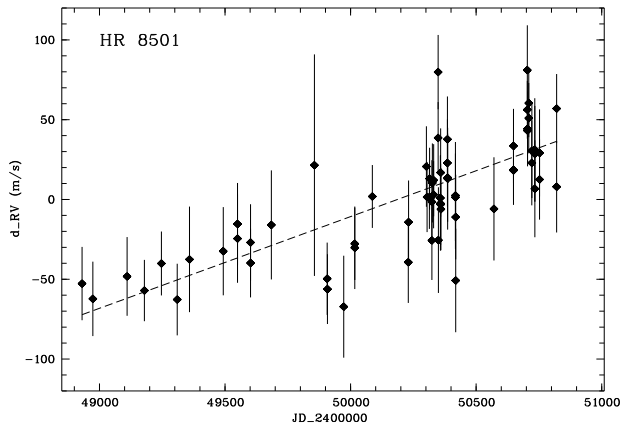


Fig. 17. Best-fit linear trend for HR 8501, the *RV* shift per day is $+0.057 \pm 0.006 \text{ ms}^{-1}$ and the rms scatter around this slope is 23.4 ms^{-1} .

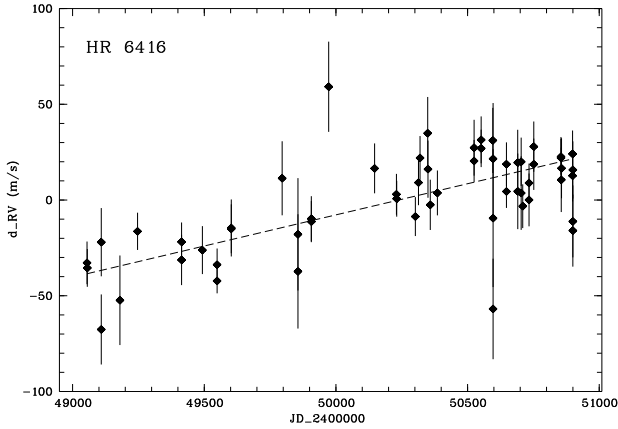


Fig. 15. Best-fit linear trend for HR 6416, the *RV* shift per day is $+0.032 \pm 0.003 \text{ ms}^{-1}$ and the rms scatter around this slope is 19.4 ms^{-1} .

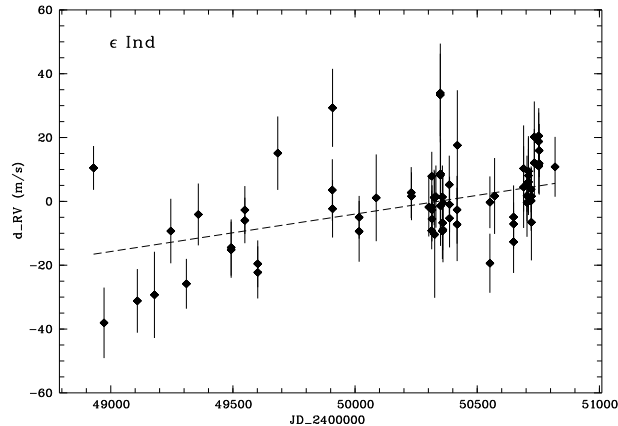


Fig. 16. Best-fit linear trend for ϵ Ind, the *RV* shift per day is $+0.012 \pm 0.002 \text{ ms}^{-1}$ and the rms scatter around this slope is 11.6 ms^{-1} .

Star	<i>RV</i> trend [$\text{ms}^{-1}\text{d}^{-1}$]	rms [ms^{-1}]
β Hyi	$+0.02 \pm 0.0024$	19.3
α For	-0.04 ± 0.007	50.9
HR 6416	$+0.032 \pm 0.003$	19.4
ϵ Ind	$+0.012 \pm 0.002$	11.6
HR 8501	$+0.057 \pm 0.005$	23.4

Table 6. Linear *RV* trends and the rms scatter around these slopes. Uncertainties of the slopes correspond to the $\chi^2 = \chi^2_{\text{best}} + 1$ range.

ter around this trend is large with $\approx 51 \text{ ms}^{-1}$. Most of this residual scatter is probably caused by the high stellar activity of α For. Another possible explanation for an increase of the *RV* scatter can be contamination of the spectra of the primary by the secondary. Due to field rotation at the Nasmyth focus of the CAT telescope, light from the close secondary also entered the CES during some observations when the slit was aligned with the binary axis. This could at least to some degree have contributed to the larger scatter (the same is true for HR 8501 with an even smaller angular separation).

Neither β Hyi nor ϵ Ind are known binary stars. The detected linear *RV* trends are thus caused by previously unknown companions. The linearity of both trends points towards distant stellar companions. However, both stars also represent candidates for having very long-period ($P > 20$ yrs) planetary companions. Follow up observations using the upgraded CES, now equipped with the Very Long Camera (VLC), and the 3.6 m telescope were already performed and are still in progress. Analysis of the new data and the combination with the *RV* results presented here will show whether the linearity of both trends continues.

4.3. Period search

To search for periodic signals in the complete RV results of the CES sample we again use the Lomb-Scargle periodogram (Lomb 1976, Scargle 1982). We estimate the False Alarm Probability (FAP) of a peak in the power spectrum by employing a bootstrap randomization method. In this bootstrap approach the actual RV measurements are randomly redistributed while keeping the times of observations fixed (Kürster et al. 1997, Murdoch et al. 1993). The major advantage of this method is the fact that the FAP-levels can be derived without any assumptions on the underlying noise distribution (like e.g. a Gaussian). We will continue to follow this bootstrap philosophy also in determining upper mass-limits for planets in Sect. 5.

The search interval is 2 to 5000 days. For each star we perform 10,000 bootstrap randomization runs to estimate the FAP of the maximum peak in the power spectrum. Since the validity of the FAP resulting from random redistribution is lower in the case of high temporal concentration at one or several points (i.e. “data clumping” when during one night a large number of measurements were taken while in other nights this number is significantly lower) we also perform the analysis on the RV set binned in nightly averages.

Table 7 summarizes the periodogram results for all survey stars (in the cases of κ For, HR 2400, HR 3677 and α Cen A & B the period search was performed on the RV residuals after subtraction of the binary orbit).

The periodogram analysis of the original RV data found periods with FAP_1 (for the original un-binned RV data set) below 0.001 at: β Hyi, τ Cet, ι Hor, α Cen A & B residuals, ϕ^2 Pav and HR 8501. However, none of them, with the exception of ι Hor and HR 8501, reveal a significant signal in their nightly averaged RV data set. In the cases of β Hyi and α Cen A & B the significance of the low FAP_1 is decreased by high temporal concentration of their RV data (the periodogram results for α Cen A & B are discussed in detail in Endl et al. 2001a). The significant $P = 5000$ day signal for HR 8501 is caused by the found linear RV trend (see Fig. 17), since 5000 days is the maximum period searched for. The same happens in the case of HR 6416, although the $P = 5000$ day signal is no longer significantly recovered in the nightly averaged data set.

Thus ι Hor remains the single case in the CES Long Camera survey which shows a convincing periodic RV variation of statistical significance due to an orbiting planet.

The results for ϕ^2 Pav are interesting, since the FAP_2 of the $P = 7$ day signal is still low with 0.003 and just marginally above the 1 permill threshold. We will discuss the case of ϕ^2 Pav later.

4.4. Activity induced RV excess scatter

Several studies (Saar & Donahue (1997), Saar et al. (1998), Santos et al. (2000), Paulson et al. (2002)) have investigated and discussed the relationship between stellar activity and RV scatter induced by activity related phenomena like surface inhomogenities (spots) and variable granulation pattern. Saar et al. (1998) found a correlation between an excess RV scatter (exceeding the expected scatter due to internal measurement uncertainties) and the rotational speed of the G and K dwarfs in the sample of the Lick planet search program. Interestingly, Paulson et al. (2002) measured simultaneously the Ca II H&K emission and RV s of members of the Hyades cluster and showed that only for a few stars (5 out of 82) the chromospheric activity is correlated with an RV excess.

In the case of the CES Long Camera survey we can estimate P_{Rot} for 13 stars, which reveal an excess RV scatter compared to their internal errors, and examine whether this excess scatter is correlated with intrinsic stellar activity. Stellar rotational periods are either taken from Saar & Osten (1997) or estimated using Eqs.(3) & (4) in Noyes et al. (1984) and the Ca II H&K results from Henry et al. (1996). Fig. 18 displays the RV excess scatter plotted vs. P_{Rot} , which shows a general increase in the excess scatter with shorter rotational periods. The sample of stars included in the diagram consist of 2 F-type stars (ζ Tuc, ν Phe), 7 G-type stars (ι Hor, ζ^2 Ret, HR 4523, HR 4979, HR 6416, HR 8323, HR 8501) and 4 K-type stars (ϵ Eri, δ Eri, α Cen B, ϵ Ind). Although we do not have P_{Rot} -values for α For and HR 8883, the observed large excess scatter for these two stars is probably also due to fast rotation and enhanced stellar activity. As already mentioned, both stars are bright X-ray sources and HR 8883 displays prominent Ca II H&K emission. This result confirms the general picture of increased RV -jitter due to enhanced stellar activity.

5. Limits for planetary companions

We now continue with the quantitative determination of the sensitivity of the CES Long Camera survey for the discovery of planets orbiting the target stars. With this we ask the question: which planets would we have detected if they existed? Since they are not detected we can exclude their presence and hence set constraints. Starting from the *null – hypothesis* that the observed RV scatter is mainly caused by measurement uncertainties and/or additional intrinsic stellar effects, we establish the planet detection threshold for each star. This detection limit for each individual target is determined by numerical simulations of planetary orbits of varying amplitudes, periods and phase angles. These simulated planetary signals can either be recovered by a periodogram significantly or not and thus deliver the quantitative upper limits.

Star	N ₁	Period ₁ [days]	Power ₁	FAP ₁	N ₂	Period ₂ [days]	Power ₂	FAP ₂
ζ Tuc	51	9.7	8.5	0.009	36	9.7	6.9	0.10
β Hyi	157	2000	28.9	<0.0001	39	3.2	6.4	0.684
HR 209	35	30.0	5.7	0.458	24	4.7	5.0	0.932
ν Phe	58	6.5	7.9	0.085	41	6.5	5.7	0.672
HR 448	24	2.0	3.0	0.79	13	6.8	4.8	0.134
HR 506	23	7.6	5.8	0.36	18	7.6	5.7	0.447
τ Cet	116	5.2	14.3	0.0002	32	5.6	7.2	0.158
κ For _{Res}	40	75.8	6.3	0.381	30	14.0	5.4	0.72
HR 753	6	3.3	2.2	0.20	3	10.7	1.0	0.827
ι Hor	95	322.6	26.7	<0.0001	57	322.6	16.2	<0.0001
α For	65	4.3	11.0	0.0013	36	4.3	7.1	0.265
ζ^1 Ret	14	6.2	3.8	0.275	8	33.1	3.0	0.368
ζ^2 Ret	58	6.4	6.7	0.5	44	2.0	6.5	0.638
ϵ Eri	66	4.4	10.2	0.0025	28	2.7	5.1	0.739
δ Eri	48	2.3	5.9	0.011	27	9.5	6.8	0.089
α Men	41	4.5	8.0	0.067	29	4.5	7.6	0.051
HR 2400 _{Res}	53	3.9	7.0	0.284	38	5.3	6.5	0.405
HR 2667	66	13.5	8.9	0.066	43	5.8	6.6	0.719
HR 3259	35	3.8	3.3	0.307	26	3.8	2.6	0.931
HR 3677 _{Res}	34	5.0	7.3	0.05	26	178.6	5.4	0.266
HR 4523	27	2.4	6.4	0.309	21	2.4	5.5	0.768
HR 4979	52	16.8	8.6	0.055	33	16.8	6.7	0.252
α Cen A _{Res}	205	16.4	19.4	<0.0001	48	16.4	7.7	0.114
α Cen B _{Res}	291	11.6	31.8	<0.0001	43	17.3	7.1	0.042
HR 5568	40	5.1	4.7	0.604	19	2.5	4.8	0.675
HR 6416	57	5000	11.4	0.001	38	5000	8.7	0.034
HR 6998	51	6.7	8.2	0.039	35	6.7	7.7	0.116
HR 7373	8	4.5	3.1	0.4651	7	4.5	2.7	0.955
HR 7703	30	7.2	6.2	0.14	21	7.2	5.8	0.295
ϕ^2 Pav	90	7.0	14.4	0.0001	41	7.0	10.1	0.003
HR 8323	20	2.1	4.5	0.464	13	2.1	4.7	0.21
ϵ Ind	73	2.6	10.0	0.017	44	2.6	7.0	0.429
HR 8501	66	5000	19.0	<0.0001	44	5000	13.1	0.0001
HR 8883	31	36.2	8.7	0.013	21	36.2	5.8	0.391
Barnard	24	2.3	5.0	0.29	15	2.3	5.1	0.015
GJ 433	15	5.4	3.5	0.417	8	5.4	3.2	0.591
Prox Cen	65	3.2	10.5	0.0012	35	3.2	6.8	0.05

Table 7. Periodogram results. Power₁, Period₁ and FAP₁ are the results of the original *RV* data set (N₁), while Power₂, Period₂ and FAP₂ gives the values for the nightly averages (N₂).

5.1. The method

Companion limits for different planet search samples were presented by Murdoch et al. (1993), Walker et al. (1995) and Cumming et al. (1999) for the Mount John Observatory, CFHT and Lick Observatory surveys, respectively. Nelson & Angel (1998) derived an analytical expression for detection limits and re-examined the CFHT data set. The sensitivity of *RV* surveys for outer planets with orbital periods exceeding the survey duration was studied in Eisner & Kulkarni (2001). They all used different approaches, most of them are based on the periodogram, to determine the detection capabilities of individual surveys. In Kürster et al. (1999b) we have already determined these limits for one target of the CES program,

namely Prox Cen, using also a different method based on a Gaussian noise term.

The method we apply to the CES data was already described in Endl et al. (2001b) and in greater detail in Endl et al. (2001a). The latter paper also includes a comparison with a method based on Gaussian noise terms and discusses the differences and the advantage of the bootstrap approach. Our bootstrap-based method can be summarized as follows: for each star we perform numerical simulations of planetary orbits with K (the *RV* semi-amplitude), ϕ the orbital phase and P (the orbital period) as model parameters (orbital eccentricity e is set to 0). The maximum period represents the time span of CES observations of the target star (with a typical duration of ≈ 2000 days). For each set of K and P 8 different orbits are created with their phase angles shifted by $\pi/4$. These signals are

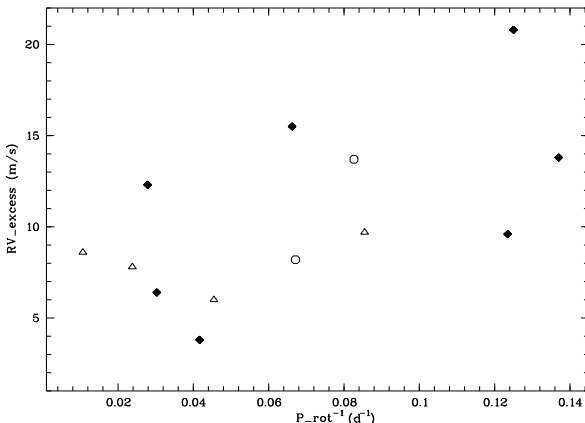


Fig. 18. Correlation between RV excess scatter and stellar rotational period. F-type stars are shown as circles, G-type stars as full diamonds and K-type as triangles. The excess scatter increases with decreasing P_{Rot} (with ι Hor having the highest value of excess scatter).

added to the *actual RV* measurements (i.e. we use our own data set as noise term) and perform a period search in the range of 2–5000 days (using the Lomb-Scargle periodogram). We define a planet as *detectable* if the period is found by the periodogram and the statistical significance of its peak in the power spectrum is higher than 99% (i.e. its false alarm probability (FAP) is lower than 0.01). If the FAP equals or exceeds 0.01 at only one of the trial phases, a planet is not classified as detectable at these P and K values. Again the FAP is estimated by using the bootstrap randomization method and for each simulated signal we perform 1000 bootstrap runs. By increasing the K parameter until the FAP is less than 1% for all orbital phases at a given P value we obtain quantitative upper limits for planetary companions. By taking as the noise-term the obtained RV results for single stars (and the RV residuals for binary stars) we assure that the noise distribution is equal to the measurement errors of the CES survey for this star (obviously, the temporal sampling of the simulated signals are identical with the real monitoring of each individual star by the CES survey). The value of the parameter K can be transformed immediately into an $m \sin i$ value and the parameter P into an orbital separation a for the companion, thus we derive an $m \sin i - a$ companion limit function. The simulations are performed in the period range of $P = 3$ days and the total duration of observation for each individual target. This period range is sampled in such a manner that companion limits are computed every 0.25 AU (i.e. a $P^{2/3}$ spacing). One exception is the 1-year window ($P = 365$ days) where the companion limit is determined additionally in every case. The derived upper mass-limits are strictly correct only at the $P \& K$ -values where the simulations are performed (circles in Figs. B.1 - B.7), the interpolated limits (dashed lines in the figures) are not mathematically stringent, since the frequency-space is too large to be sampled completely

Star	Mass [M_{\odot}]	Star	Mass [M_{\odot}]
ζ Tuc	1.06 ¹	HR 3259	0.9
β Hyi	1.1 ²	HR 3677	2.1
HR 209	1.1	HR 4523	1.04
ν Phe	1.2	HR 4979	1.04
HR 448	1.23 ¹	HR 5568	0.71
HR 506	1.17	HR 6416	0.89
τ Cet	0.89	HR 6998	1.0
κ For	1.12	HR 7703	0.74
α For	1.2	ϕ^2 Pav	1.1 ¹
ζ^2 Ret	1.1	ϵ Ind	0.7
ϵ Eri	0.85 ³	HR 8501	1.04
δ Eri	1.23 ¹	HR 8883	2.1
α Men	0.95	Barnard	0.16 ⁴
HR 2400	1.2	GJ 433	0.42
HR 2667	1.04		

Table 8. Assumed stellar masses for the companion limit determination. If not otherwise stated the mass estimates are taken from Gray (1988) for the according spectral type. Other references: 1. Porto de Mello, priv. comm., 2. Dravins et al. (1998), 3. Drake & Smith (1993) 4. based on the mass-luminosity relation from Henry et al. (1999).

(i.e. two times for each independent frequency = *Nyquist* criterion).

The following stars are excluded from the limit determination due to insufficient observations: HR 753 (with only 6 RV measurements), HR 7373 (8 RV measurements), and ζ^1 Ret (14 RV measurements). Another exclusion is ι Hor, where the planet was discovered, and the α Centauri system, in which case companion limits based on the CES data have already been presented in Kürster et al. (1999b) for Proxima and in Endl et al. (2001a) for α Cen A & B.

5.2. Stellar masses

In order to transform the obtained K value of detectable RV signals into an $m \sin i$ value for planetary companions using Kepler's third law, we have to assume a certain mass for the host star. The stellar mass values we take for the $m \sin i$ calculations are summarized in Table 8. As an example for the dependence of the $m \sin i$ values on the stellar mass value, we take the case of β Hyi ($1.1 M_{\odot}$). For an orbital period of $P = 44$ days an error of $0.1 M_{\odot}$ leads to a small uncertainty in the $m \sin i$ of $\pm 0.03 M_{\text{Jup}}$ and at a period of $P = 1890$ days the corresponding value is larger with $\pm 0.13 M_{\text{Jup}}$.

5.3. Windows of non-detectability

There are two special cases which can render a simulated signal totally undetectable (using the criteria described above). These windows of non-detection are displayed in the figures as vertical lines which bracket a gap in the companion limits.

5.3.1. Insignificant signal

In the first case the data structure (total number of observation and sampling density) leads to the effect that for a certain phase angle the FAP of the input signal always exceeds the 1% level regardless of the increase of the K parameter. This is the case for the gaps seen in the limits for instance for HR 209 at 2.25 AU (Fig. B.1) and for HR 506 at the same separation (Fig. B.2).

5.3.2. Aliasing

However, for most cases of non-detectability we find that due to aliasing the maximum power in the periodogram for certain phase angles is not located at the input period, again, regardless of the increase in K . The seasonal 1 year period is a typical window interval for every astronomical observing program and the problem of aliasing will occur if the signal is not properly sampled within this interval (in general sampling on irregular time basis can reduce the occurrence of aliasing).

This occurs for instance in the cases of HR 3259, β Hyi, τ Cet, α Men and HR 4523, where the maximum power is found at the $1/2$ P -value for input signals with P close to the seasonal 1 year period. The peaks in the power spectrum are significant (i.e. $\text{FAP} > 0.01$) but at the wrong P -values. In other cases the maximum power is found at a completely different P value for a certain orbital phase (e.g. at 2.9 days instead of the input value of 1425 days for HR 4523).

In a conservative approach we declare these cases as non-detections since the correct parameters of the planetary signal were not recovered (remember that one undetected signal out of the eight trial phases is sufficient to define a planet as *undetectable* although seven out of eight signals were successfully recovered). One would conclude though that a planet with the wrong orbital period is present and the correct period of its orbit remains unknown (though continued monitoring of this star would eventually lead to the correct orbital parameters).

5.4. Resulting companion limits

The derived upper mass-limits for planets orbiting the CES survey stars are displayed in appendix B for each individual star. The horizontal dotted line in each plot shows (for better comparison) the $m \sin i = 1.0$ M_{Jup} border. For most of the stars the CES limit line crosses this border at orbital separations less than 1 AU. This clearly demonstrates the need for a longer time baseline as well as a better RV measurement precision to detect 'real' Jupiters at 5.2 AU.

The α Centauri system represents a special case in this limit-analysis: it allows the combination of observational constraints for planetary companions with dynamical limitations for stable orbits within the binary. In Endl et al. (2001a), paper II of this series, we have combined the CES limits with the results from the dynamical stability

study of Wiegert & Holman (1997) which led to strong constraints for the presence of giant planets orbiting α Cen A or B. Upper limits for giant planets around the third member of the α Centauri system, Prox Cen, based on the results of a different RV analysis of the CES data were presented in Kürster et al. (1999b). We therefore didn't include the plots for these 3 stars in this paper and refer the reader to the former articles.

In the cases of β Hyi and τ Cet we have nights where a great number of spectra were taken in a short consecutive time. In order to distribute the sampling more evenly and to reduce the total number of RV measurements to save CPU time, we averaged the numerous RV measurements in those nights, to get a maximum number of 3 observations per night. This reduced the total number of measurements for β Hyi to 94 (instead of 157) and for τ Cet to 62 (instead of 116).

The results for HR 448 are limited by the short monitoring time span of 438 d and the small number of observations (24 RV measurements). For this star only companion limits for orbital separations of $a < 0.15$ AU were found.

The candidate for a planetary companion to ϵ Eri (from Hatzes et al. 2000) is also indicated in Fig. B.3 by an asterisk. It lies well inside the non-detectable region of the CES survey for this star. As described in Hatzes et al. (2000) the combination of several different RV data sets was necessary to find the signal of this companion. Moreover, the orbital period of 7 years is longer than the duration of the CES Long Camera survey.

For the binaries κ For, HR 2400 and HR 3677 the simulated planetary signal is added to the original RV set, which still possess the huge variation due to the binary orbits. Thus, one additional step in the limit determination has to be performed. Before the periodogram analysis is started we subtract the binary motion (the preliminary Keplerian solution and trends from Sect. 3) by minimization of the χ^2 -function. The same is done for the low-amplitude trends of α For, HR 6416 and HR 8501 caused by their stellar secondaries. Again the found trends are subtracted (by χ^2 -minimization) from the synthetic RV sets and the periodogram analysis is performed on the RV residuals.

HR 5568 was only observed for 384 days and companion signals with periods > 250 days ($a \approx 0.7$ AU) were not detected at all orbital phases. The CES monitoring of HR 7703 spans over 1042 days and no gaps were found in the detectability of planetary companions within this time-frame (maximum separation $a \approx 1.75$ AU).

For HR 8323 we detected only 3 test signals at $P = 3, 123$ and 224 days, at all other P -values the test orbits were not recovered. This low detectability is due to the smaller number of observations (20 RV measurements) and the shorter time span of monitoring (1068 d). The results for HR 8323 are not displayed.

The numerous gaps in the CES detectability of companions of the giant HR 8883 (G4III) are a direct result of

the large RV scatter (65.2 m s^{-1}) and the irregular monitoring of this star (see Fig. B.7).

In the case of GJ 433 (M2V) the small number of RV measurements (15) and the short duration of monitoring (337 days) prohibit determination of companion limits. No simulated planetary signal could be detected at *all* orbital phases at the trial periods of 3, 10, 40, 100, 150, 175, 250 and 333 days. Only at the trial period of 200 days a signal with a K amplitude of 600 m s^{-1} was detected, corresponding to a companion of $m \sin i = 9.8 \text{ M}_{\text{Jup}}$ with a semi-major axis of $a = 0.5 \text{ AU}$.

Barnard's star (M4V) constitutes another special case of the companion limit analysis. The limits determined from the CES RV data can be combined with the astrometric companion limits based on the HST Fine Guidance Sensor (Benedict et al. 1999). This combination is very effective since both methods are complementary to each other (the RV method is more sensitive to close-by companions while for astrometry the detectability of more distant companions is better). Fig. B.7 displays the companion limits derived from the CES data and combined with HST astrometric results. These combined limits demonstrate that - except for an *aliasing*-window near $a = 0.08 \text{ AU}$ (corresponding to $P = 20$ to 27 d) - *all* planets with $m \sin i > 1.2 \text{ M}_{\text{Jup}}$ can be excluded.

5.5. Orbital eccentricity

One limitation of this method is the restriction to sinusoidal signals ($e = 0$), i.e. planetary system similar to our Solar System. The huge parameter space for eccentric orbits (including the two additional parameters of orbital eccentricity e and anomaly ω) simply makes it impossible to sample all possible orbits at a given period P . The main motivation of examining the validity of the derived limits also for eccentric orbits is of course the fact that many extrasolar planets with longer periods known today have eccentric orbits.

5.5.1. The test case: HR 4979

In order to check the validity of the derived $e = 0$ limits also for eccentric orbits we select the special test case of HR 4979 and compare the limits for $e = 0$ orbits for certain sets of K and P values with $e > 0$ orbits. HR 4979 was chosen because the companion limits for this star are a smooth function without gaps (see Fig. B.5). We want to emphasize that the following tests can only serve as an example and the results cannot be taken as generally valid for the complete survey. Furthermore, due to the above mentioned feasibility limitations, the sampling rate of the parameter space has to be kept low (e.g. the parameter ω is sampled only every 90°). The test consists of the two following steps:

1. Simulations are performed, where the orbital phase ϕ is kept fixed and the parameters P, e , and ω are varied, to obtain a rough estimate of the $e > 0$ limits validity.

2. For the smallest and largest P -value, the orbital phase parameter ϕ is also varied and the detectability is determined for these cases.

For step 1 we create 110 simulated orbits with different e and ω values at the trial periods $P = 46, 130, 365, 1045$, and 1452 days (with a fixed value of orbital phase angle ϕ), and the K semi-amplitude of $22, 20, 35, 26$, and 30 m s^{-1} (these values represent the limits obtained for the $e = 0$ case). For each parameter-set of P, K and e we simulate 4 different orbits with ω shifted by 90° . Again, we perform for each simulated signal 1000 bootstrap runs to obtain the FAP level. A signal is classified as *non-detected* if the FAP exceeds 1% or the periodogram shows maximum power at a different period than the input value P . Fig. 19 displays the detectability of these test signals as a function of orbital eccentricity. For smaller values of P these signals get undetectable at $e = 0.5$ and 0.6 , while longer periodic signals are detectable until $e = 0.8$. The lower detectability at shorter periods might be explained by the fact that with increasing eccentricity the duration of the RV maxima (minima) of the orbits is getting smaller than typical observational time intervals. For longer periods these maxima or minima are better sampled than for short periods and hence better detectable for the periodogram.

In step 2 the orbital phase ϕ is introduced as additional parameter for two selected P -values (the minimum and maximum value of P : 46 & 1452 d). For each set of P, K, e and ω values the parameter space of ϕ is additionally sampled 5 times (equidistant). This means that for each pair of P and e parameter 20 synthetic planetary signals are generated (at 4 different ω and 5 different ϕ values). Fig. 20 shows the result of this second test. The general form of the results from the first test is preserved.

These tests illustrate - at least in the case of HR 4979 - that the $e = 0$ limits appear to be valid for longer periods and eccentricities of $e < 0.6$, while for smaller P values the validity is constrained to low eccentricities.

5.6. Average detection threshold

By computing the ratio $F(P)$:

$$F(P) = \frac{K_{\text{detected}}[\text{m s}^{-1}]}{\text{RV scatter}[\text{m s}^{-1}]} \quad (1)$$

with P the trial period, K_{detected} the semi-amplitude of the detected RV signal and the RV -scatter as the individual noise-term of the star and by taking the mean ratio \bar{F}_{Star} for all P -values where an upper mass limit was determined we obtain an average detection threshold for each star. For the 30 stars, where we determined companion limits, and at all P -values we found $F(P) > 1.$, except in the case of β Hyi where $F(3 \text{ d}) = 0.8$ (which also demonstrates the detectability of signals with smaller amplitude than the measurement precision by a sufficient number of datapoints). The main bulk of values of $F(P)$ lies in the range from 1.2 to 4, with an average value of 2.75 (\bar{F}_{CES})

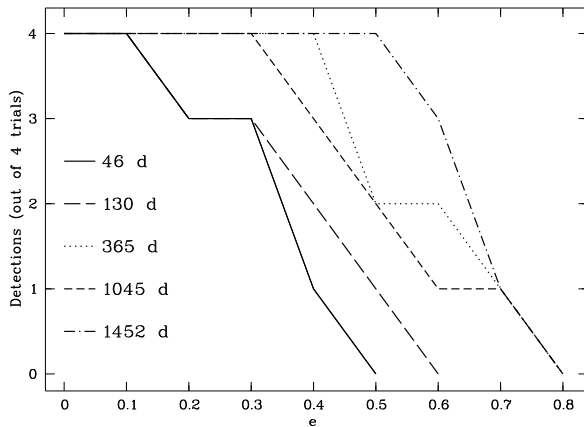


Fig. 19. Eccentricity-test part 1: Detectability of $e > 0$ orbits in the case of HR 4979 and fixed orbital phase. For each trial period and eccentricity 4 different orbits (ω shifted by 90°) are created with the K -value obtained from the sinusoidal simulations. The graph shows how many of the 4 test signals are detected. The detectability increases with orbital period. For the shortest period $P = 46$ days the detectability ends at $e = 0.5$ (no test signal is recovered) and for the longer periods at $e = 0.8$.

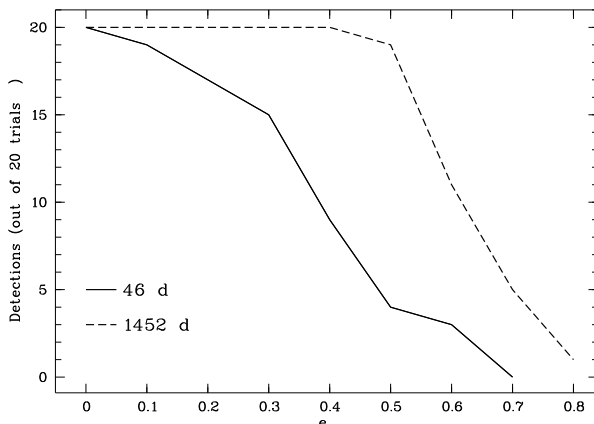


Fig. 20. Eccentricity-test part 2: Detectability of $e > 0$ orbits for HR 4979 at $P = 46$ and 1452 d with the orbital phase ϕ varied. For each pair of P and e 20 synthetic orbits at the 4 different ω -values, each with 5 different ϕ -values, are created. The plot displays how many of the 20 signals are recovered successfully. The general form of Fig. 19 is preserved.

for all 30 stars and P -parameter values where companion limits were derived.

The value of \bar{F}_{CES} corresponds to the average of the RV signals detected and does not represent the exact average detection threshold of the CES survey due to the presence of the non-detectability gaps, which cannot be taken into account in this statistic. Table 9 gives the average detection factor for each star (\bar{F}_{Star}) and the result-

Star	F_{Star}	K [m s^{-1}]	Star	F_{Star}	K [m s^{-1}]
ζ Tuc*	3.3	71.3	HR 3259*	2.26	36.7
β Hyi*	1.76	35.2	HR 3677	2.44	56.8
HR 209*	5.37	124	HR 4523*	3.57	53.6
ν Phe	2.16	38.6	HR 4979	1.66	23.2
HR 448*	16.4	280.3	α Cen A	1.88	22.2
HR 506*	3.79	90.5	α Cen B	2.14	26.9
τ Cet*	1.95	22.6	HR 5568*	2.58	19.9
κ For	2.42	34.5	HR 6416	1.77	34.3
α For	1.85	94.2	HR 6998	2.67	52.4
ζ^2 Ret	2.04	44.4	HR 7703	2.8	37.3
ϵ Eri*	2.67	40.0	ϕ^2 Pav	2.25	79.5
δ Eri	2.12	32.9	ϵ Ind	3.35	45.2
α Men*	2.51	24.6	HR 8501*	1.73	40.4
HR 2400	1.69	42.0	HR 8883*	5.67	369.4
HR 2667	1.54	25.4	Barnard*	4.58	170.5

Table 9. Average detection threshold \bar{F}_{Star} and resulting mean \bar{K} -amplitudes of detectable planetary signals for each star. Stars indicated with an asterisk (*) possess windows of non-detectability.

ing mean \bar{K} -amplitude of detectable planetary signals (the presence of non-detectability gaps is also indicated).

The minimum value of \bar{F}_{Star} was found for HR 2667 ($\bar{F}_{\text{Star}} = 1.54$) and the highest value for HR 448 ($\bar{F}_{\text{Star}} = 16.4$). In terms of average detectable K -amplitude the minimum for the CES Long Camera survey is 19.9 m s^{-1} for HR 5568, which is not surprising since this is the star with the smallest RV -scatter ($\text{rms} = 7.7 \text{ m s}^{-1}$), and the maximum at 369.4 m s^{-1} for the highly variable star HR 8883.

Fig. 21 compares these CES-survey mean \bar{K} -amplitudes of detectable planetary signals with the K -amplitudes of known extrasolar planets as a function of $B-V$. For this purpose we selected only K -amplitudes less than 100 m s^{-1} (which excludes three CES stars: HR 448, HR 8883 and Barnard's star and 27 known extrasolar planets). Except for CES stars with $B-V < 0.6$, most of the RV -signals of the known extrasolar planets are within the detection range of the CES Long Camera survey.

Fig. 22 shows a comparison of our numerical simulations with an analytic detection threshold for a False Alarm Probability of 0.01 by using Eq.(15) from Cochran & Hatzes (1996). The theoretical curve (solid line in Fig. 22) is calculated on the basis of the Lomb-Scargle periodogram and gives the S/N -ratio ($F = K/\sigma$) of signals detected with $\text{FAP} \leq 0.01$ as a function of number of measurements N . Clearly, the plot shows that virtually *no* signals can be detected with $N < 20$, consistent with our results, and that the curve constitutes a clear lower limit to our “real” detectability (circles in Fig. 22). It is not surprising that the detected signals do not get closer to the theoretical limit, since they had to be recovered at *all* phase angles. In many cases the CES Long Camera survey successfully recovered signals at certain phase angles

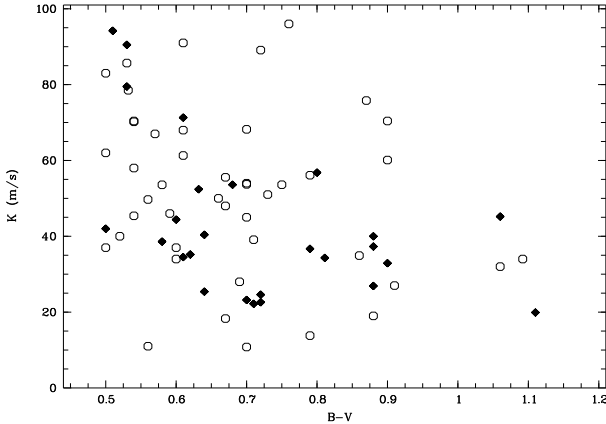


Fig. 21. Average detectable K-amplitudes of the CES-survey (diamonds) as a function of $B - V$, compared to K-amplitudes of known extrasolar planets (circles). Only K-amplitudes less than 100 m s^{-1} are displayed (excluding HR 448, HR 8883 and Barnard's star). The list of amplitudes of the known extrasolar planets was compiled using the information on the websites of the Geneva observatory program (<http://obswww.unige.ch/~udry/planet/planet.html>) and the California & Carnegie planet search (<http://exoplanets.org/>) and the colors were derived from the SIMBAD database. Except for the blue part of the diagram (stars with $B - V < 0.6$) most of the known extrasolar planets are located within the detection range of the CES Long Camera survey.

at lower F -values, which are not included in Fig. 22 due to the above mentioned criterion. Fig. 22 demonstrates again that the sensitivity of RV planet search programs can also be improved by increasing N , i.e. by taking more data, beside raising the RV precision.

5.7. Mass range

The lowest companion mass which was detected during our simulations corresponds to an $m \sin i = 0.079 \text{ M}_{\text{Jup}} \approx 0.27 \text{ M}_{\text{Saturn}}$ or $25 \text{ M}_{\text{Earth}}$ planet in a $P = 3 \text{ d}$ and $a = 0.036 \text{ AU}$ orbit around HR 5568. Fig. 23 shows the lower section of the limiting $m \sin i$ -values of all simulated planetary signals which were determined as detectable by the CES survey. Planets with $m \sin i = 1 \text{ M}_{\text{Jup}}$ were found undetectable for the 30 CES survey stars at separations larger than 2 AU. However, at small orbital separations of $a \approx 0.04 \text{ AU}$ the CES survey would have detected “51 Peg”-type planets in *all* cases and for 22 survey stars even the presence of sub-Saturn-mass planets. The bias of RV planet searches towards short-period planets is obvious in Fig. 23. Also indicated in Fig. 23 is the location of the planet discovered around ι Hor. With $m \sin i = 2.26 \text{ M}_{\text{Jup}}$ and $a = 0.925 \text{ AU}$ ι Hor b clearly lies above the main part of the limiting detectable $m \sin i$ -values and was thus “easily” detectable by the CES Long Camera survey.

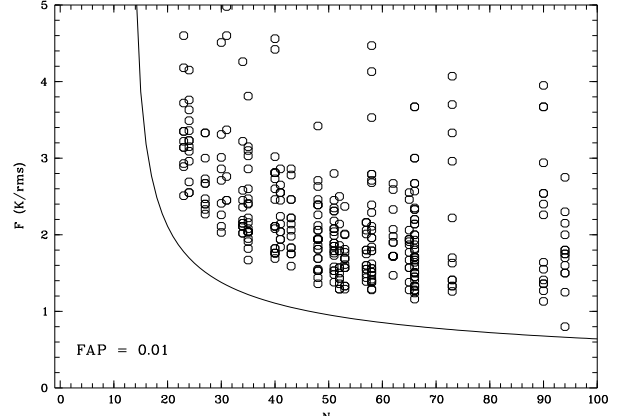


Fig. 22. Comparison of detected simulated signals (circles) with an analytically derived detection threshold (solid line) based on the Lomb-Scargle periodogram and a False Alarm Probability (FAP) of 0.01 (using Eq.(15) in Cochran & Hatzes 1996). F denotes the S/N -ratio of the signal in the power spectrum and N the total number of measurements per star.

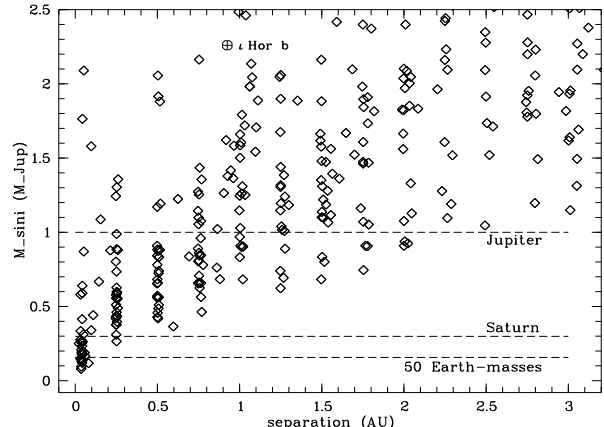


Fig. 23. Lower section of all detectable $m \sin i$ -values (diamonds) of the CES Long Camera survey. The horizontal dashed lines show the mass values of Jupiter, Saturn and a hypothetical 50 Earth-mass planet. The location of ι Hor b ($m \sin i = 2.26 \text{ M}_{\text{Jup}}$, $a = 0.925 \text{ AU}$) is also indicated. ι Hor b lies well above the main bulk of detectable $m \sin i$ -values. At orbital separations larger than 2 AU no planets with $m \sin i < 1 \text{ M}_{\text{Jup}}$ are detectable. For 22 stars the detectable $m \sin i$ -value at $a \approx 0.04 \text{ AU}$ reach down into the sub-Saturn mass regime ($m \sin i < 0.3 \text{ M}_{\text{Jup}}$).

6. Discussion

The planet around ι Hor remains the single clear detection of an extrasolar planet by the CES Long Camera survey. This corresponds to a detection rate of $\approx 3\%$, a value similar to other precise Doppler searches. The discovery of ι Hor b demonstrated for the first time the feasibility of the RV technique in planet detection in the case of young and thus moderately active stars.

Seven stars (19%) of the CES sample show minor signs of variability (minor in the sense that they pass one but fail at other tests): ζ Tuc, HR 506, ζ^2 Ret, ϵ Eri, ϕ^2 Pav and HR 8883. While for ϵ Eri this is an indication for the presence of the highly eccentric RV signature of the planet, the cause of variability for the other stars remains unknown since no convincing periodicity or trends were found. For HR 8883 the *RV* variations can be explained by the high intrinsic activity of this star (high X-ray luminosity).

Low amplitude linear *RV* trends were found for the following 5 targets (14%): β Hyi, α For, HR 6416, ϵ Ind and HR 8501. For the known binaries α For, HR 6416 and HR 8501 these trends agree well with the expected acceleration by the stellar secondary. The large scatter around the linear trend of α For is probably also due to high stellar activity (again a high X-ray luminosity).

β Hyi and ϵ Ind are identified as candidates for having long-period and probably stellar companions. But could these trends also be caused by planets? If we assume that the minimum orbital period would be 4 times the monitoring time span (i.e. $P \approx 20$ years) and that the *RV* semi-amplitude is of the order of the *RV* shift over the 5 years (β Hyi: 38 m s^{-1} , ϵ Ind: 21 m s^{-1}) and $e = 0$, the observed trends could be caused in the case of β Hyi by a planet with $m \sin i \approx 4 \text{ M}_{\text{Jup}}$ at $a \approx 7.6 \text{ AU}$ and for ϵ Ind by an $m \sin i \approx 1.6 \text{ M}_{\text{Jup}}$ companion at $a \approx 6.5 \text{ AU}$. Such planetary systems with a distant giant planet would resemble our Solar System more closely than the extra-solar planetary systems found so far. For $e > 0$ orbits the period can even be much shorter than 20 years and we therefore conclude that although the linearity of the *RV* trends points towards distant and previously unknown stellar companions, both stars constitute prime targets for follow-up observations by the CES planet search program.

ϕ^2 Pav has been earlier announced by our team as a possible candidate for having a planetary companion with an orbital period of about 43 days and $m \sin i = 0.7 \text{ M}_{\text{Jup}}$ (Kürster et al. 1999a). This signal was found with a low confidence level and based on a preliminary analysis of a subset of the Long Camera data, using an early version of the *Radial* code (Cochran & Hatzes 1990) to obtain the *RV* measurements. The analysis of the complete data set of ϕ^2 Pav using the *Austral* software did not confirm the presence of this companion. The total rms scatter over the entire 5 1/2 years is 35.4 m s^{-1} , slightly larger than the mean internal error of 31.3 m s^{-1} for this star. No apparent Keplerian signal is present. This is consistent with results coming from the Anglo-Australian planet search (Butler et al. 2001), who collected 7 measurements of ϕ^2 Pav over the course of 1 year, which reveal a total rms scatter of only 5 m s^{-1} (the Anglo-Australian planet search uses the UCLES echelle spectrometer which covers a much larger spectral region and the entire 1000 \AA of the I_2 -reference spectrum, hence the higher precision of their results). However, we have identified in our much longer and higher sampled data a periodic signal of ≈ 7 days, again with low confidence (the FAP of this signal

is still higher than 0.001 but it appears in both the unbinned original *RV* data as well as in the nightly averaged results). If the periodic signal is indeed real what could produce such an *RV* signature? ϕ^2 Pav belongs to the ζ Ret stellar kinematic group, a group of metal deficient stars with an age of ≈ 5 Gyr (del Peloso et al. 2000). The iron abundance was determined as $[\text{Fe}/\text{H}] = -0.37$ by Porto de Mello & da Silva (1991) and as $[\text{Fe}/\text{H}] = -0.44$ by Edvardsson et al. (1993). This low metallicity can account for the observed large *RV* scatter, since fewer and shallower absorption lines in the small CES bandpass degrade our measurement precision. In fact ϕ^2 Pav has the second largest internal *RV* error of the F-type stars in the CES sample. Based on $H\alpha$ emission, ϕ^2 Pav appears to be slightly more active than the Sun (del Peloso et al. 2000) and the star is already evolving into the subgiant phase (Porto de Mello & da Silva 1991). With this higher level of activity we suspect that the $P = 7$ day *RV* variation is in fact the stellar rotation period and that our *RV* measurements are affected by cool spots in the photosphere of ϕ^2 Pav. These spots would modulate the *RV* measurements with a typical timescale of P_{Rot} . Since these spots appear and disappear on short timescales compared to the monitoring duration and the overall activity level might change over 5 1/2 years, the amplitude as well as the phase of this modulation varies with time. Such a signal is therefore difficult to detect significantly, which is exactly what we observe here. The expected size of the subsurface convection zone for a low-metallicity F-type star is smaller than for a star of solar metallicity. Even with $P_{\text{Rot}} = 7$ days such a star would not display a much larger activity level than ϕ^2 Pav due to the inefficiency of the dynamo. From the $v \sin i = 6.7 \text{ km s}^{-1}$ and $R_* = 1.86 R_{\odot}$ (Porto de Mello priv. comm.) and the P_{Rot} value of 7 days we derive a viewing angle of $\approx 30^\circ$. The continued monitoring of ϕ^2 Pav will demonstrate whether the $P = 7$ day is robust and can be recovered with a higher confidence level.

Roughly 50% of the targets (18 stars) of the CES Long Camera survey show absolutely no sign of variability or trends in their *RV* data. Within the given *RV* precision of the CES Long Camera survey the following stars were found to be *RV*-constant: HR 209, HR 448, HR 753, ζ^1 Ret, δ Eri, HR 2667, HR 4523, HR 4979, HR 6998, HR 7373, HR 7703, HR 8323 and GJ 433.

In the cases of the binaries κ For, HR 2400, HR 3677 and α Cen A & B (see Endl et al. 2001a) no sign of significant periodic signals were found in the *RV* residuals after subtraction of the binary orbit. Interestingly, κ For does not show any excess scatter although based on its L_X -flux and $H\alpha$ -emission (Porto de Mello priv. comm.) it is an active star. Still, the residuals after subtraction of the binary orbit are consistent with our measurement errors.

The CES Long Camera survey is in *all* cases sensitive to short-period (“51 Peg”-type) planets with orbital separations of $a < 0.15 \text{ AU}$. This result confirms the general bias of precise Doppler searches towards short-period companions. For 22 stars of the CES Long Camera survey

these mass-limits reach down into the sub-Saturn mass regime at $a \approx 0.04$ AU.

For most stars the region where planets with $m \sin i < 1 M_{Jup}$ could have been detected is confined to orbital separations of less than 1 AU. Beyond 2 AU no planets with $m \sin i \approx 1 M_{Jup}$ were found to be detectable around any star of the survey. Subsequently, in order to detect a Solar System analogue the time baseline and (if possible) the RV precision of the CES planet search has to be increased. Within the limitations of our numerical simulations ($e = 0$, $P^{2/3}$ sampling) we can rule out the presence of giant planets within 3 AU of the CES survey stars according to the limits presented here (with the exceptions of HR 209, HR 8883 and periods inside the non-detectability windows).

Spectral leakage is the main cause for the windows of non-detectability. Even for well observed stars like e.g. τ Cet or β Hyi these windows exist close to the seasonal one year period. This demonstrates how difficult the detection of RV signals with a one year periodicity is.

The average detection threshold F_{CES} for the examined 30 Long Camera survey stars is 2.75, meaning that on average detectable planetary signals have K amplitudes which exceed the noise level by a factor of 2.75.

6.1. Outlook

With the decommissioning of the Long Camera in April 1998, phase I of the CES planet search program came to an end. All results based on this homogeneous set of observations are included in this work or were already presented earlier.

Although the CES was modified quite substantially after that, with the installation of the Very Long Camera (VLC) yielding a higher resolving power of $R \approx 220,000$ and an optical fibre-link to the 3.6 m telescope being the most significant changes, the CES planet search program was continued using the same I_2 -cell for self-calibration. This ensures the capability to merge the RV results from phase I with the newer phase II data set without the need to compensate for velocity zero-point drifts as demonstrated for HR 5568 in Fig. 24. The displayed RV results now cover almost 3 years for this star (compared to 1 year of the Long Camera survey). For the intermediate time when the 1.4 m CAT and the 3.6 m telescope were used in combination with the VLC and the 2K CCD (which meant a reduced bandwidth of ≈ 18 Å due to the higher spectral dispersion) we observe a small RV offset of ≈ 25 m s $^{-1}$. This offset can be explained by the difference in spectral regions which were analysed to obtain the RV s. However, after the VLC was equipped with a longer 4K CCD the spectral bandwidth was increased to 36.5 Å. To assure that the RV results are based on the same spectral regions we analyse both the Long Camera and the VLC data using a stellar template spectrum obtained with the most current instrumental setup (i.e. VLC & 4K CCD). A comparison of the RV results derived with the current

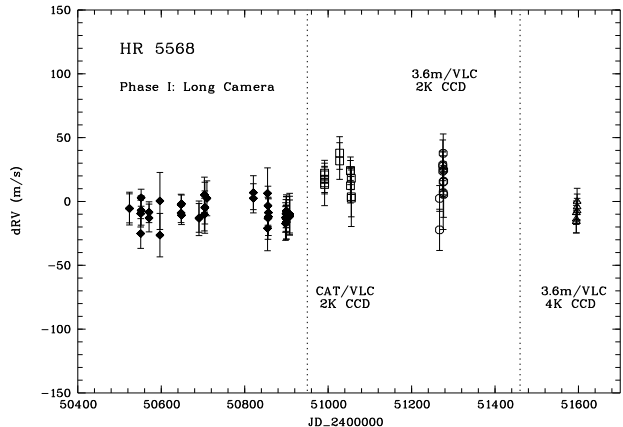


Fig. 24. RV monitoring of HR 5568 during the refurbishment of the CES. A comparison of the Long Camera results (full diamonds) with data collected with the new VLC and the 2K CCD (boxes and circles) show a slight offset. This offset disappears with the installation of the 4K CCD (triangles) which increased and equalized the spectral bandwidth (see text for details). The total rms scatter over the 3 years is 15.5 m s $^{-1}$, and 7.5 m s $^{-1}$ without the intermediate data (between the vertical dotted lines).

CES and Long Camera results does no longer show any velocity offset (see Fig. 24). This demonstrates that the I_2 -cell technique successfully compensates even for major instrumental setup changes. This guarantees a high long-term RV precision and allows a smooth continuation of the CES planet search program.

The Very Long Camera at the CES is promising to increase the RV precision of the CES planet search due to several reasons: the resolving power is doubled with respect to the Long Camera while the spectral bandwidth is not reduced by a large amount (36.5 Å instead of 48.5), and the S/N -ratio of spectra is higher due to the usage of image-slicers and the larger aperture of the 3.6 m telescope. With the successful merging of the new Very Long Camera data with the Long Camera survey and an expected better RV precision the CES planet search might become sensitive to Solar System analogues in the near future.

7. Summary

1. We present more than 5 years of high precision differential radial velocities of 37 stars in the southern hemisphere observed with the 1.4 m CAT telescope and the CES spectrograph in Long Camera configuration.
2. In this sample of stars we detected 1 extrasolar planet around the young and active G-dwarf ι Hor. The results for ϵ Eri contribute to the evidence for a long-period planetary companion.
3. κ For, HR 2400 and HR 3677 were found to be spectroscopic binaries with orbital periods significantly longer

than the duration of the Long Camera survey. For all three stars the *RV* residuals after subtraction of the binary motion are consistent with our measurement errors.

4. We identified low-amplitude linear *RV* trends for α For, HR 6416 and HR 8501 in agreement with their long-period binary orbital motion. In the cases of β Hyi and ϵ Ind we detected low-amplitude linear *RV* slopes of unknown origin.
5. A period search within the complete *RV* data set did not reveal another significant periodic signal beside the planetary signal of ι Hor b and in the case of HR 8501 a signal with $P > 5000$ days indicating the found linear *RV* trend for this star.
6. We set quantitative upper mass-limits for planets orbiting the CES Long Camera survey stars based on our long-term *RV* data and numerical simulations of planetary signatures.
7. Based on these mass-limits we can exclude the presence of short-period Jupiter-type planets around all examined survey stars, while planets with $m \sin i < 1$ M_{Jup} outside of 2 AU were undetectable by the CES Long Camera survey.
8. Except for CES targets with $B-V < 0.6$, a comparison of our simulation results with the *RV*-signals of known extrasolar planets shows that most of these planets could have been detected by the CES Long Camera survey.
9. We demonstrate that the I₂-cell technique successfully compensates for the instrumental changes at the CES after April 1998 and that a smooth continuation of the CES planet search program is guaranteed. The increase in time baseline as well as a possible better *RV* precision with the Very Long Camera data will allow us to become sensitive to planetary systems more similar to our own Solar System.

Acknowledgements. We are thankful to the ESO OPC for generous allocation of observing time to the CES planet search program and to the ESO night assistants and support staff at La Silla and Garching (during remote observing runs). Our referee Stephane Udry had many important comments which helped to improve this article significantly. We would also like to thank Gustavo F. Porto de Mello, who contributed with many valuable discussions on the stellar properties of the CES target stars. ME and SE both acknowledge support by the ESO science office, ME was also supported by the Austrian Fond zur Förderung der wissenschaftlichen Forschung Nr. S7302 and SE under E.U. Marie Curie Fellowship contract HPMD-CT-2000-00005. ME, APH and WDC acknowledge support from NSF Grant AST-9808980 and NASA Grant NAG5-9227. During most of the time for this work MK was employed by the European Southern Observatory whose support is gratefully acknowledged. This work made use of the online SIMBAD database.

References

Benedict, G.F., McArthur, B., Chappell, D.W., Nelan, E., Jefferys, W.H., Van Altena, W., Lee, J., Cornell, D., Shelus, P.J., Hemenway, P.D., Franz, O.G., Wasserman, L.H., Duncombe, R.L., Story, D., Whipple, A.L., & Fredrick, L.W. 1999, AJ, 118, 1086

Butler, R.P., Marcy, G.W., Williams, E., McCarthy, C., Dosanjh, P., & Vogt, S.S. 1996, PASP, 108, 500

Butler, R.P., Tinney, C.G., Marcy, G.W., Jones, H.R.A., Penny, A.J., & Apps, K. 2001, ApJ, 555, 410

Campbell, B., Walker, G.A.H., & Yang, S. 1988, ApJ, 331, 902

Cochran, W.D., & Hatzes, A.P. 1990, in Proc. Optical spectroscopic instrumentation and techniques for the 1990s - Applications in astronomy, chemistry, and physics; Las Cruces, NM, June 4-6, 1990 (A91-51460 22-35). ed. W.A. Bellingham, SPIE1318, 148

Cochran, W.D., & Hatzes, A.P. 1996, Ap&SS, 241, 43

Cumming, A., Marcy, G.W., & Butler, R.P. 1999, ApJ, 526, 890

del Peloso, E.F., da Silva, L., & Porto de Mello, G.F. 2000, A&A, 358, 233

Drake, J.J., & Smith, G. 1993, ApJ, 412, 797

Dravins, D., Lindegren, L., & VandenBerg, D.A. 1998, A&A, 330, 1077

Edvardsson, B., Andersen, J., Gustafsson, B., Lambert, D.L., Nissen, P.E., & Tomkin, J. 1993, A&A, 275, 101

Eisner, J.A., & Kulkarni, S.R. 2001, ApJ, 550, 871

Endl, M., Kürster, M., & Els, S. 2000, A&A, 362, 585

Endl, M., Kürster, M., Els, S., Hatzes, A.P., & Cochran, W.D. 2001a, A&A, 374, 675

Endl, M., Kürster, M., Els, S., Hatzes, A.P., Cochran, W.D., Dennerl, K., Döbereiner, S. 2001b, in Proc. Planetary Systems in the Universe, IAU Symp. 202, eds. A.J. Penny, P. Artymowicz, A.-M. Lagrange, & S.S. Russell, *in press*

ESA 1997, The Hipparcos and Tycho Catalogues, ESA SP-1200

Fischer, D., Marcy, G.W., Butler, R.P., Laughlin, G. & Vogt, S.S. 2001, ApJ, *submitted*

Gray, D.F. 1988, in Lectures on Spectral-Line Analysis: F,G, and K Stars, Aylmer Express Ltd., Ontario, ISBN 0-9693532-0-0

Hatzes, A.P., Kürster, M., Cochran, W.D., Dennerl, K., & Döbereiner, S. 1996, J. Geophys. Research (Planets), 101, 9285

Hatzes, A.P., Cochran, W.D., McArthur, B., Baliunas, S.L., Walker, G.A.H., Campbell, B., Irwin, A.W., Yang, S., Kürster, M., Endl, M., Els, S., Butler, R.P., & Marcy, G.W. 2000, ApJ 544, L145H

Henry, T.J., Soderblom, D.R., Donahue, R.A., & Baliunas, S.L. 1996, AJ, 111, 439

Henry, T.J., Franz, O.G., Wasserman, L.H., Benedict, G.F., Shelus, P.J., Ianna, P.A., Kirkpatrick, J.D., & McCarthy, D.W. 1999, ApJ, 512, 864

Hünsch, M., Schmitt, J.H.M.M., & Voges, W. 1998, A&ASS, 127, 251

Hünsch, M., Schmitt, J.H.M.M., Sterzik, M.F., & Voges, W. 1999, A&ASS, 135, 319

Kasting, J.F., Whitmire, D.P., & Reynolds, R.T. 1993, Icarus, 101, 108

Kürster, M., Hatzes, A.P., Cochran, W.D., Pulliam, C.E., Dennerl, K., & Döbereiner, S. 1994, The ESO Messenger, 76, 51

Kürster, M., Schmitt, J.H.M.M., Cutispoto, G., & Dennerl, K. 1997, A&A, 320, 831

Kürster, M., Hatzes, A.P., Cochran, W.D., Dennerl, K., Döbereiner, S., Endl, M., & Vannier, M. 1998, in Proc. Workshop "Science with Gemini", eds. B. Barbuy, E. Lapasset, R. Baptista, & R. Cid Fernandes, IAG-USP & UFSC 1998, ISBN 85-85047

Kürster, M., Hatzes, A.P., Cochran, W.D., Dennerl, K., Döbereiner, S., & Endl, M. 1999a, in Proc. Precise Stellar Radial Velocities, IAU Coll. 170, ASP Conf. Ser. 185, eds. J.B. Hearnshaw, & C.D. Scarfe, 154

Kürster, M., Hatzes, A.P., Cochran, W.D., Döbereiner, S., Dennerl, K., & Endl, M. 1999b, A&A, 344, L5

Kürster, M., Endl, M., Els, S., Hatzes, A.P., Cochran, W.D., Döbereiner, S., & Dennerl, K. 2000, A&A, 353, L33

Lomb, N.R. 1976, Ap&SS, 39, 477

Marcy, G.W., & Butler, R.P. 1996, ApJ, 464, L147

Marcy, G.W., Cochran, W.D., & Mayor, M. 2000, in Protostars and Planets IV, Book - Tucson: University of Arizona Press; eds V. Mannings, A.P. Boss, & S.S. Russell, 1285

Marcy, G.W., Butler, R.P., Fischer, D., Vogt, S.S., Lissauer, J.J., & Rivera, E.J. 2001, ApJ, 556, 296

Mayor, M., & Queloz, D. 1995, Nature, 378, 355

Mayor, M., Naef, D., Pepe, F., Queloz, D., Santos, N.C., Udry, S., & Burnet, M. 2000, in Proc. Planetary Systems in the Universe, IAU Symp. 202, eds. A.J. Penny, P. Artymowicz, A.-M. Lagrange, & S.S. Russell, *in press*

Murdoch, K.A., Hearnshaw, J.B., & Clark, M. 1993, ApJ, 413, 349

Naef, D., Mayor, M., Pepe, F., Queloz, D., Santos, N.C., Udry, S., & Burnet, M. 2001, A&A, 375, 205

Nelson, A.F., & Angel, J.R.P. 1998, ApJ, 500, 940

Nidever, D.L., Marcy, G.W., Butler, R.P., Fischer, D.A., & Vogt, S.S. 2002, ApJ, *submitted*

Noyes, R.W., Hartmann, L.W., Baliunas, S.L., Duncan, D.K., & Vaughan, A.H. 1984, ApJ, 279, 763

Paulson, D.B., Saar, S.H., Cochran, W.D., & Hatzes, A.P. 2002, AJ, *in press*

Porto de Mello, G.F., & da Silva, L. 1991, AJ, 102, 1816

Queloz, D., Henry, G.W., Sivan, J.P., Baliunas, S.L., Beuzit, J.L., Donahue, R.A., Mayor, M., Naef, D., Perrier, C., & Udry, S. 2001, A&A, 379, 279

Saar, S.H., & Donahue, R.A. 1997, ApJ, 485, 319

Saar, S.H., & Osten, R.A. 1997, MNRAS, 284, 803

Saar, S.H., Butler, R.P., & Marcy, G.W. 1998, ApJ, 498, L153

Santos, N.C., Mayor, M., Naef, D., Pepe, F., Queloz, D., Udry, S., & Blecha, A. 2000, A&A, 361, 265

Scargle, J.D. 1982, ApJ, 263, 835

Valenti, J.A., Butler, R.P., & Marcy, G.W. 1995, PASP, 107, 966

Walker, G.A.H., Walker, A.R., Irwin, A.W., Larson, A.M., Yang, S.L.S., & Richardson, D.C. 1995, Icarus, 116, 359

Wiegert, P.A., & Holman, M.J. 1997, AJ, 113, 1445

Appendix A: Radial velocity results

RV results for all CES Long Camera survey stars are displayed for comparison in the same time frame (JD 2,448,800 to JD 2,451,000), and with the y-axis adjusted according to the individual velocity dispersion.

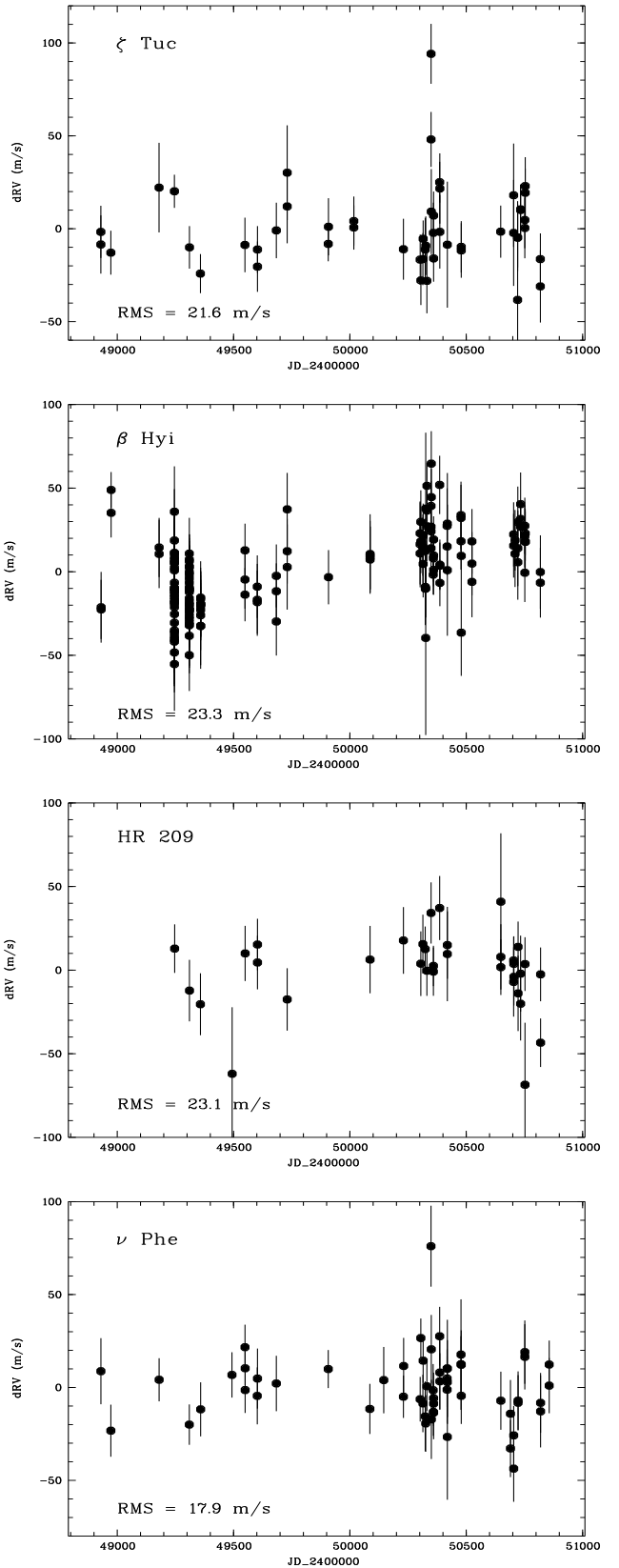


Fig. A.1. Radial velocity results for ζ Tuc, β Hyi, HR 209 and ν Phe.

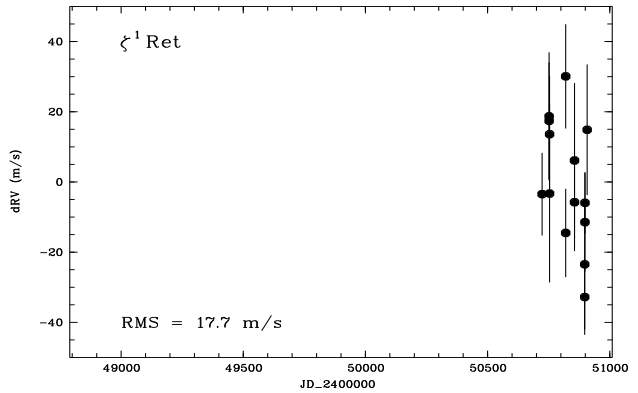
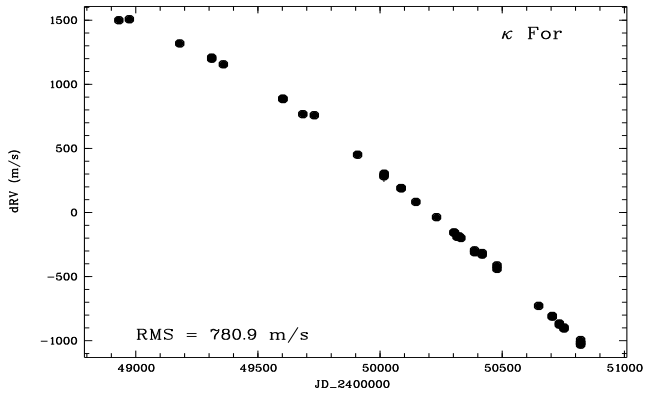
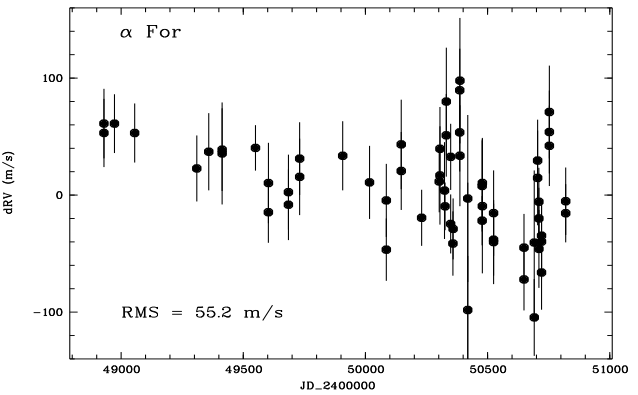
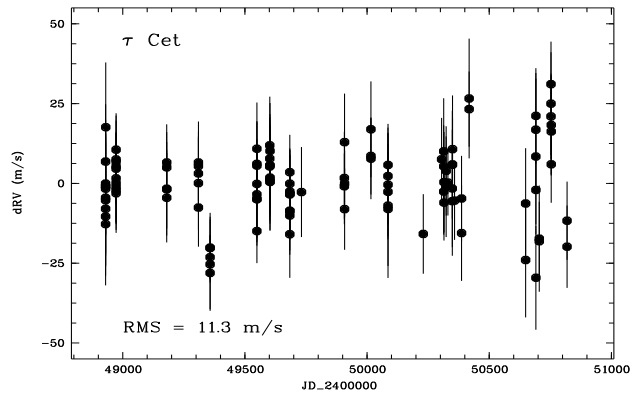
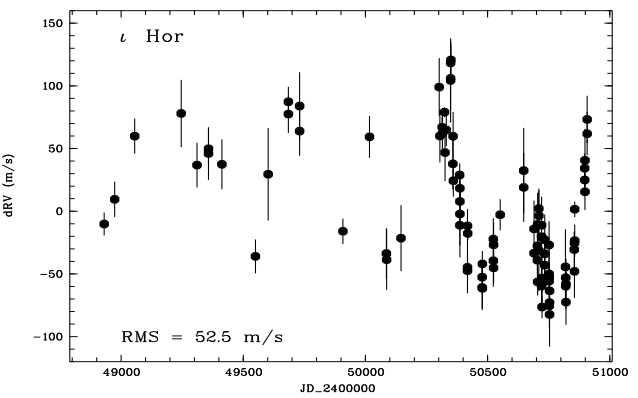
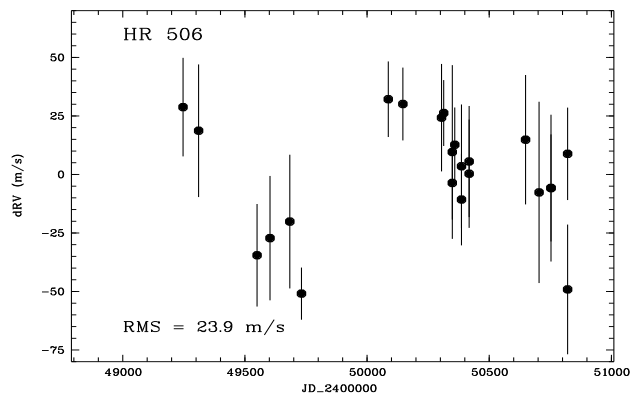
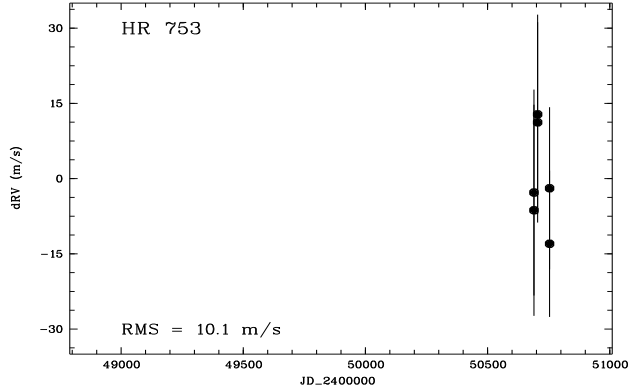
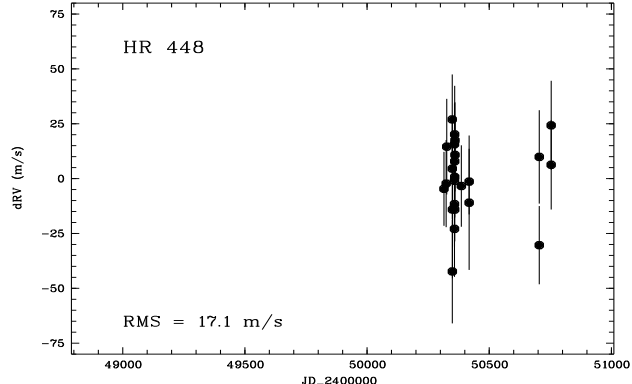


Fig. A.2. Radial velocity results for HR 448, HR 506, τ Cet and κ For.

Fig. A.3. Radial velocity results for HR 753, ι Hor, α For and ξ^1 Ret.

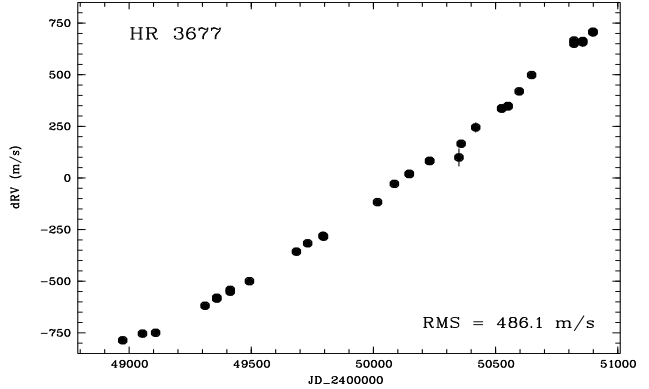
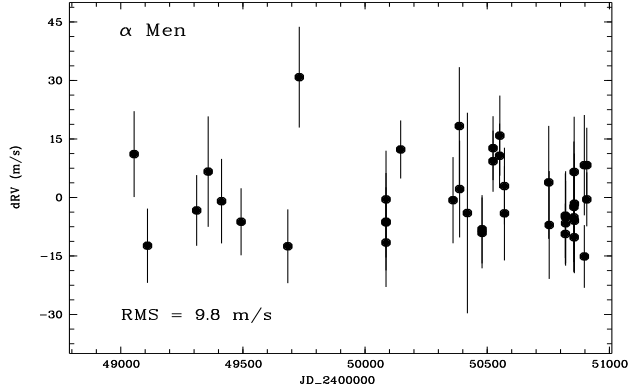
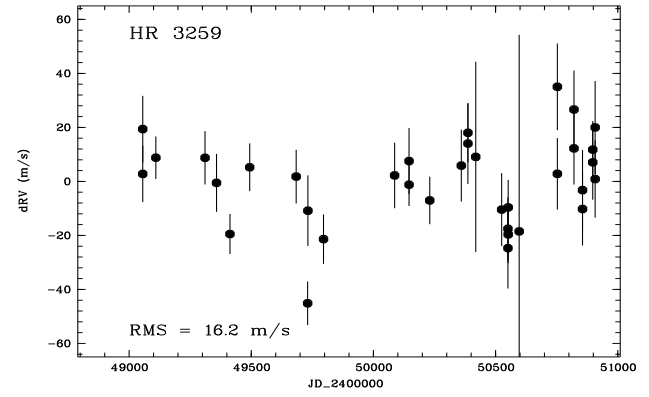
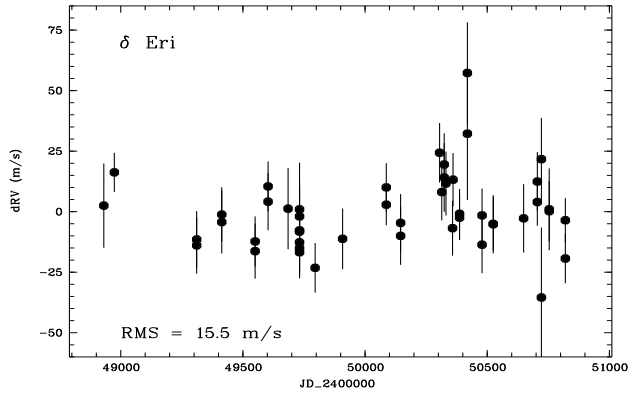
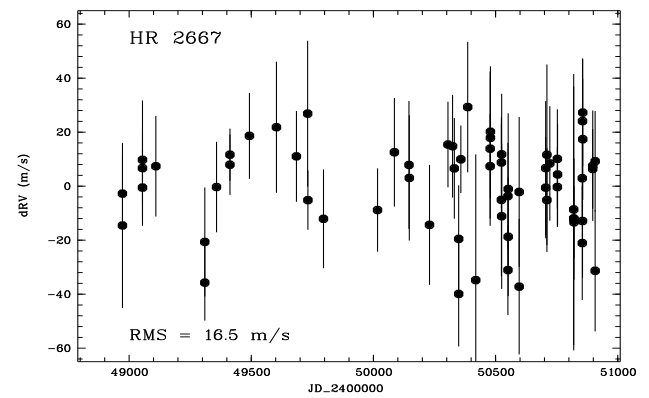
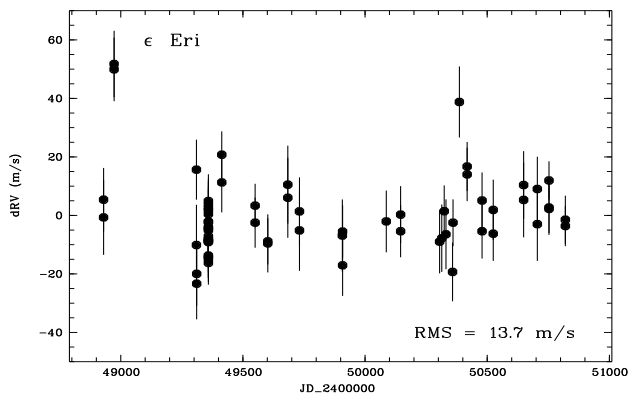
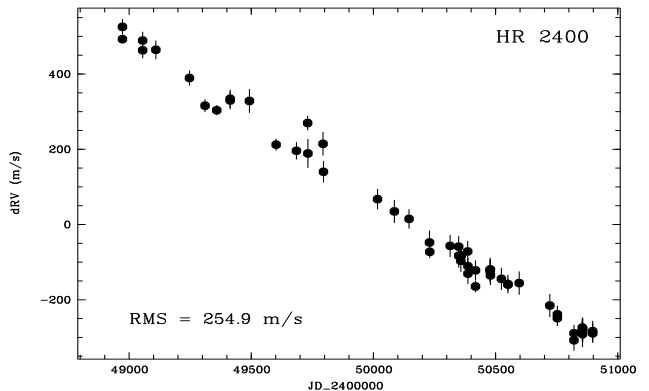
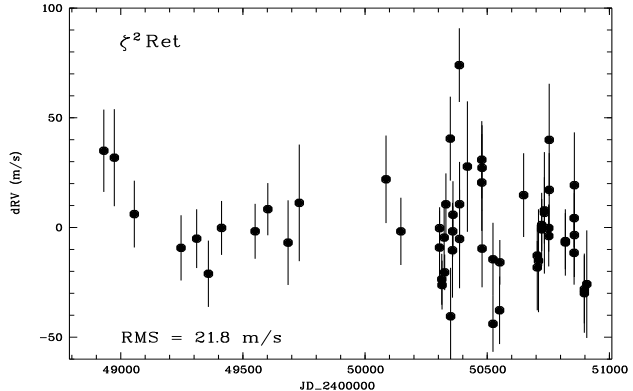


Fig. A.4. Radial velocity results for ζ^2 Ret, ϵ Eri, δ Eri and α Men.

Fig. A.5. Radial velocity results for HR 2400, HR 2667, HR 3259 and HR 3677.

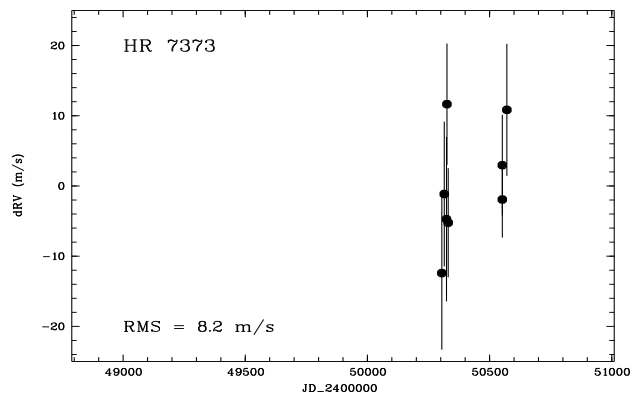
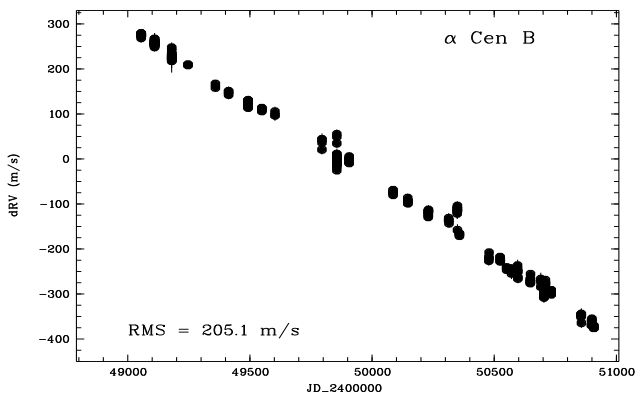
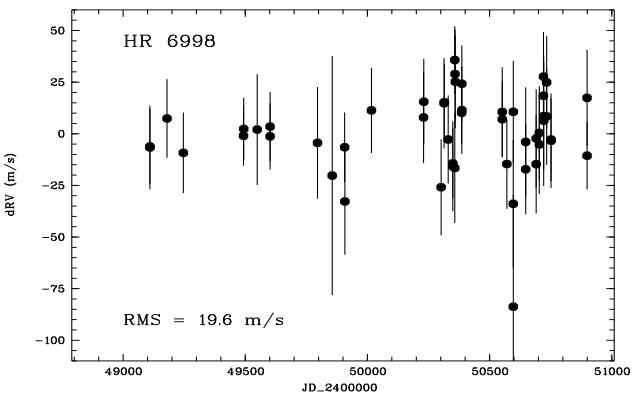
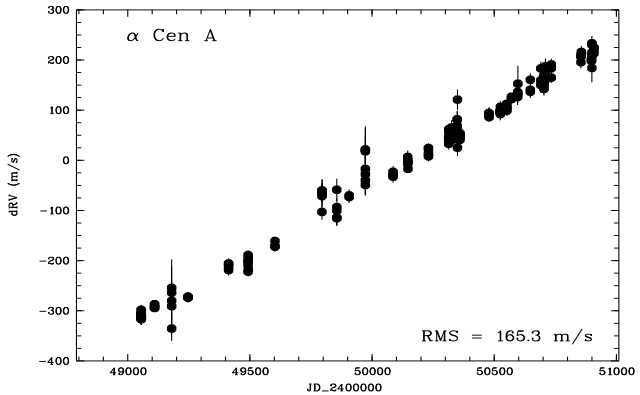
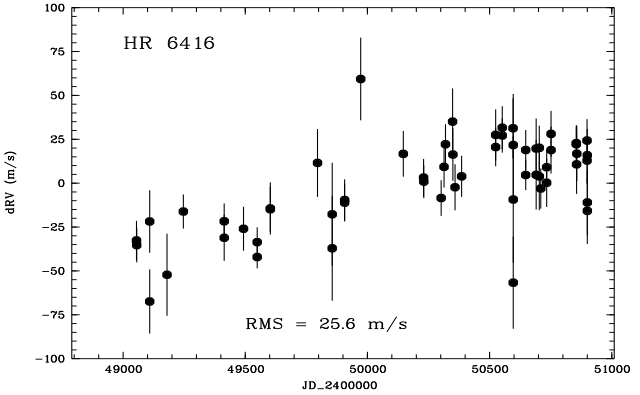
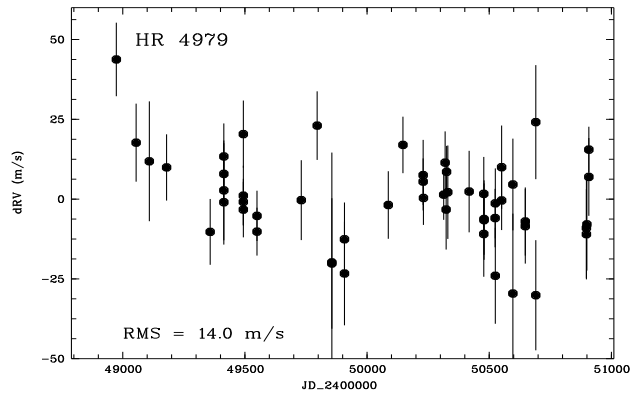
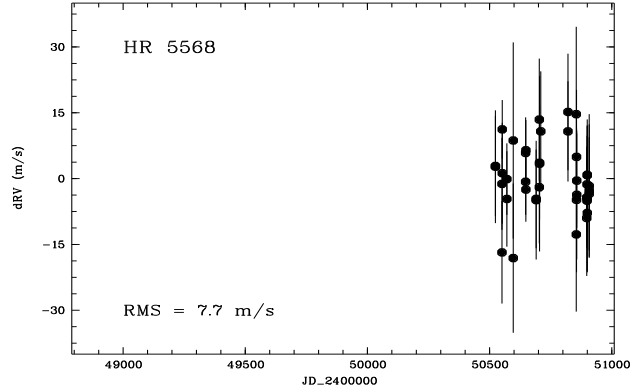
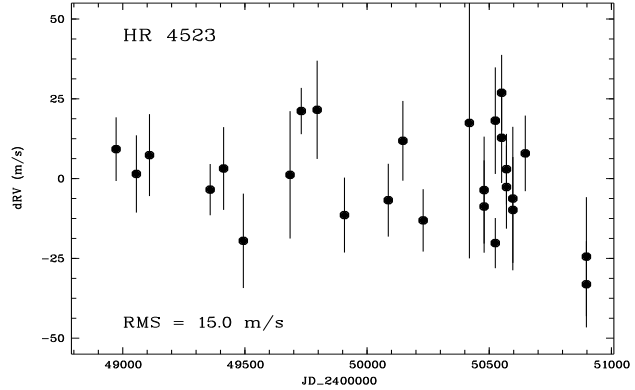


Fig. A.6. Radial velocity results for HR 4523, HR 4979, α Cen A and α Cen B.

Fig. A.7. Radial velocity results for HR 5568, HR 6416, HR 6998 and HR 7373.

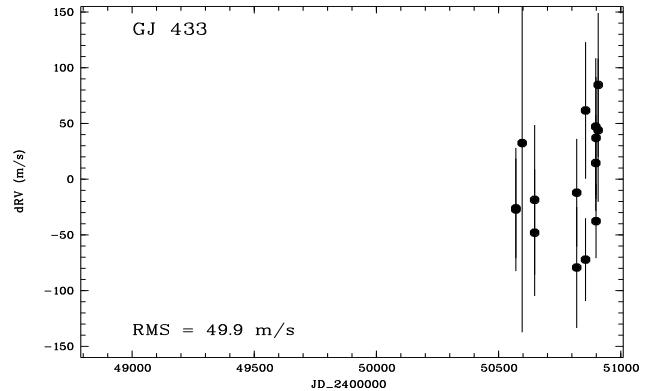
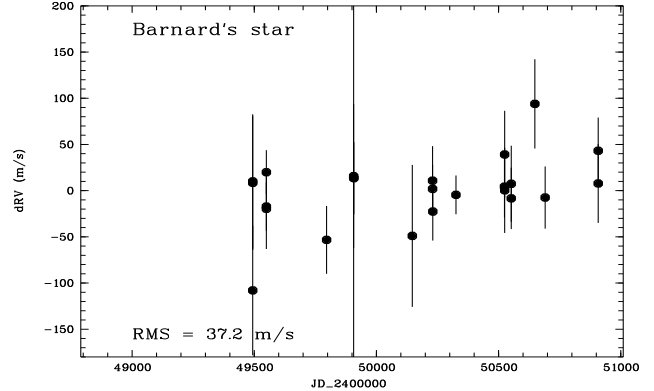
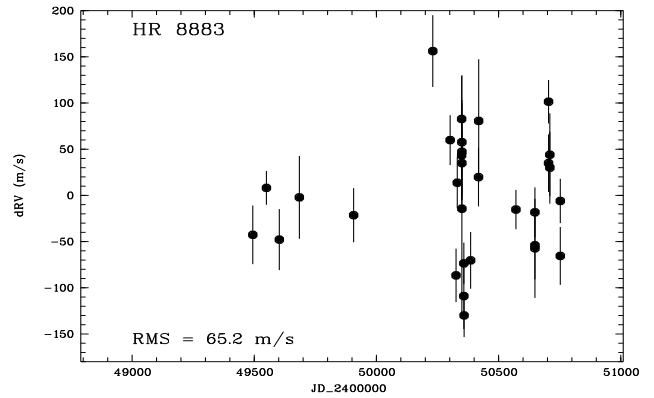
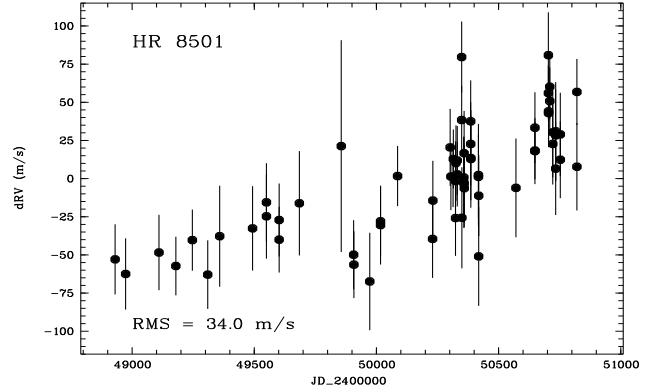
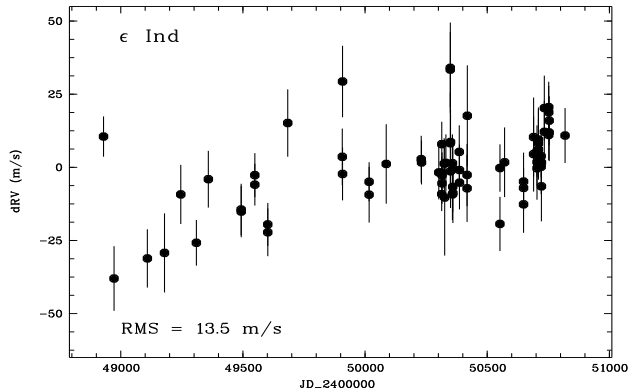
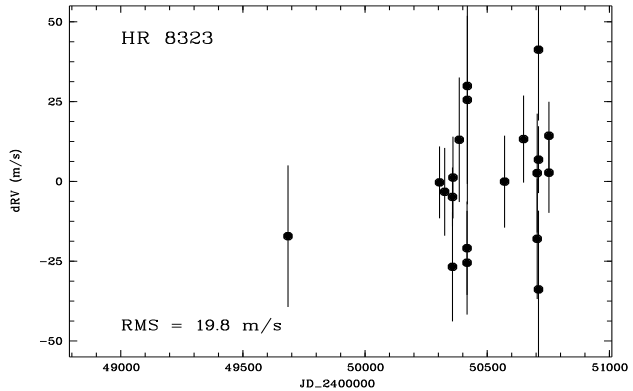
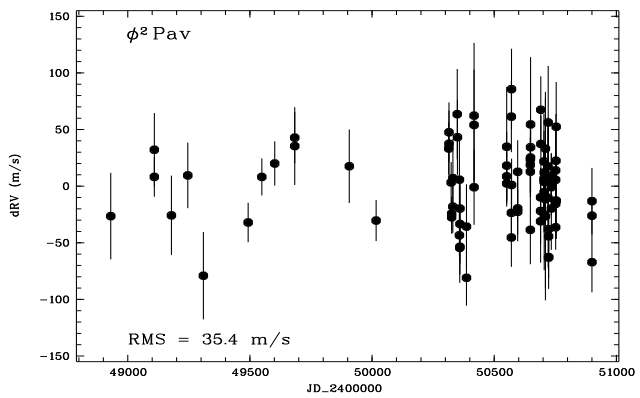
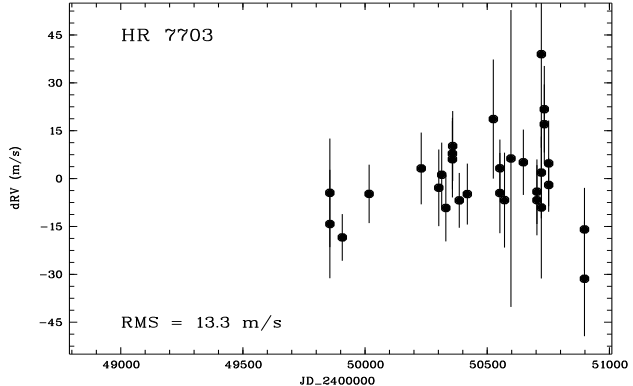


Fig. A.8. Radial velocity results for HR 7703, ϕ^2 Pav, HR 8323 and ϵ Ind.

Fig. A.9. Radial velocity results for HR 8501, HR 8883, Barnard's star and GJ 433.

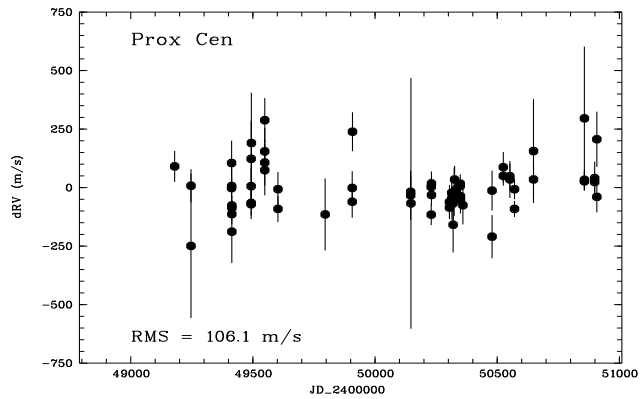


Fig. A.10. Radial velocity results for Proxima Centauri.

Appendix B: Limits for planetary companions

The upper mass-limits for planets we can place according to the method described in Sect. 5 are shown here for the 28 examined CES survey stars (the limits for planets orbiting either α Cen A or B were presented in Endl et al. (2001a). Fig. B.1 to Fig. B.7 display the $m \sin i$ values (in units of Jupiter masses) of detectable planetary signals as circles plotted vs. separation in AU. We can exclude all planets in circular orbits with masses above these limits. As described in Sect. 5 some stars have windows of non-detectability which are plotted as vertical lines. The $m \sin i = 1 M_{\text{Jup}}$ border is shown for a better comparison as horizontal dotted line in each figure.

In the case of ϵ Eri the location of the long-period planetary companion from Hatzes et al. (2000) is also indicated (Fig. B.3) by an asterisk. For Barnard's star (Fig. B.7) we include the HST astrometric limits from Benedict et al. (1999).

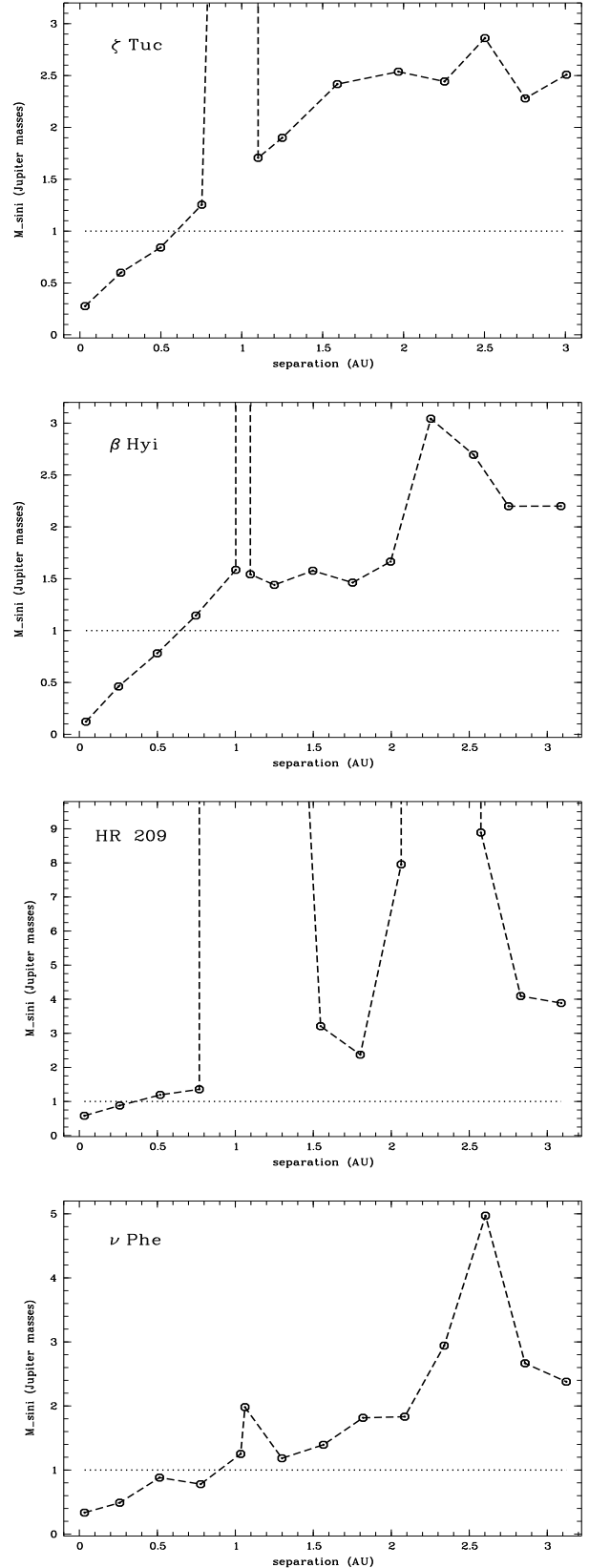


Fig. B.1. Planetary companion limits for ζ Tuc, β Hyi, HR 209 and ν Phe.

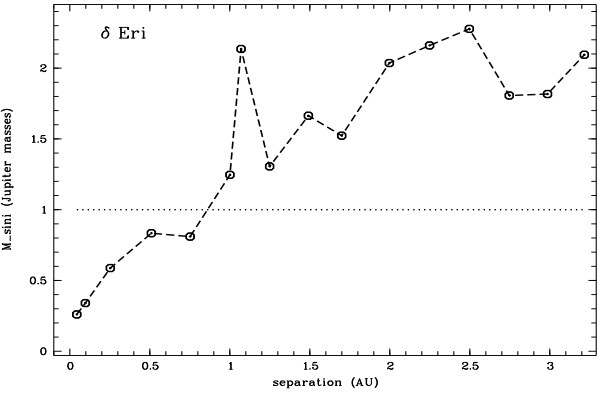
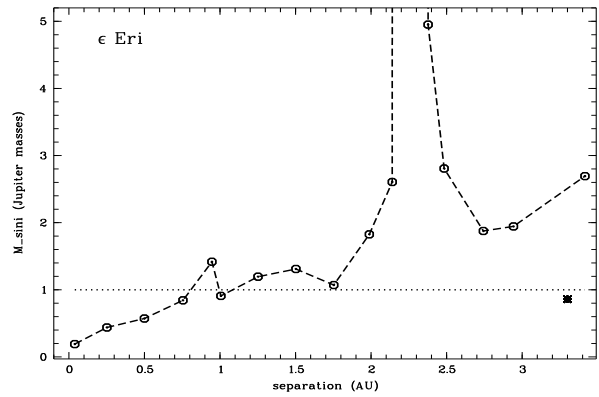
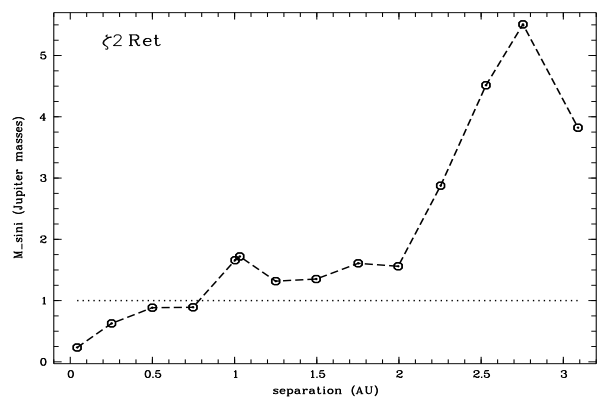
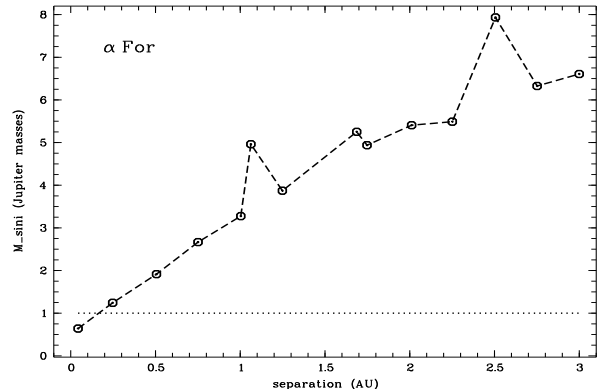
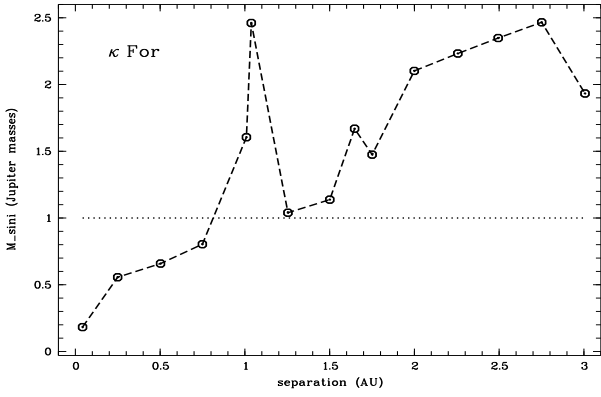
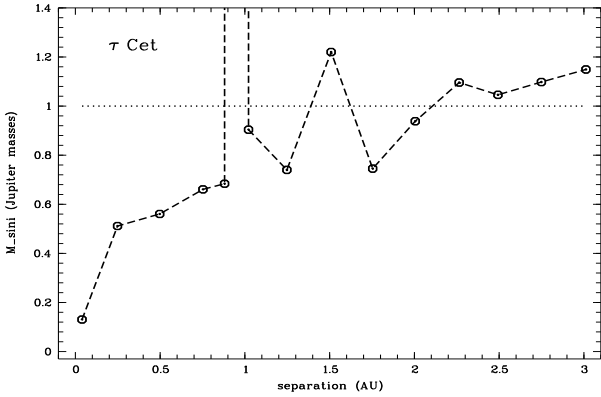
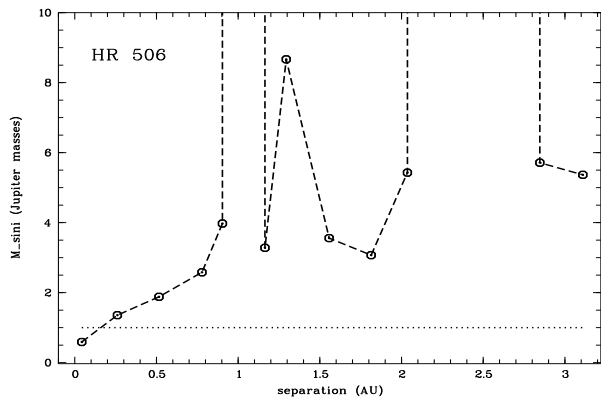
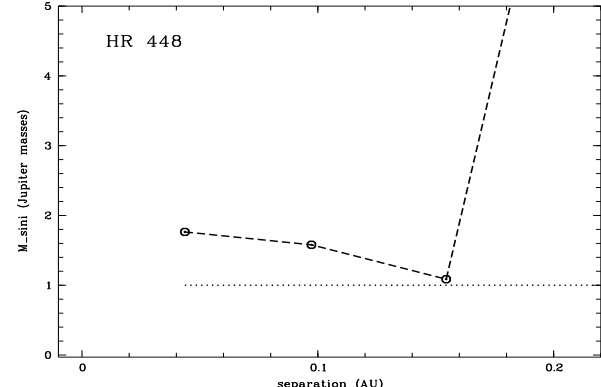


Fig. B.2. Planetary companion limits for HR 448, HR 506, τ Cet and κ For.

Fig. B.3. Planetary companion limits for α For, ζ^2 Ret, ϵ Eri and δ Eri.

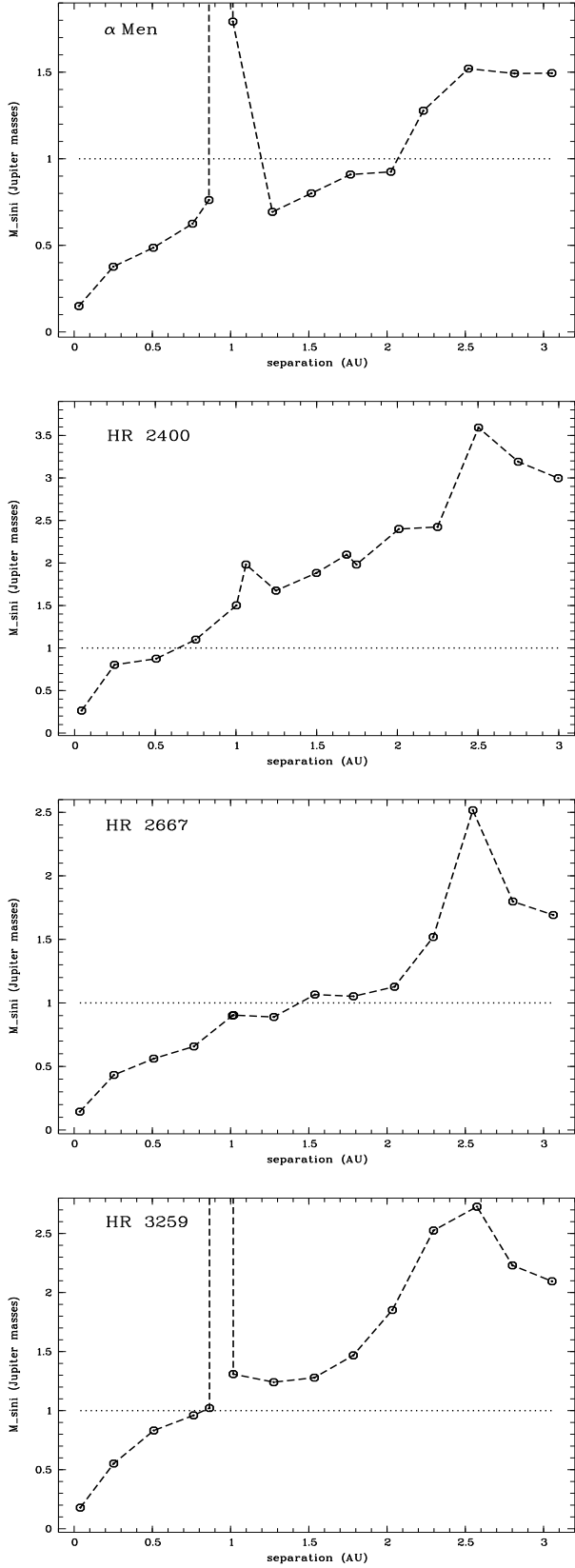


Fig. B.4. Planetary companion limits for α Men, HR 2400, HR 2667 and HR 3259.

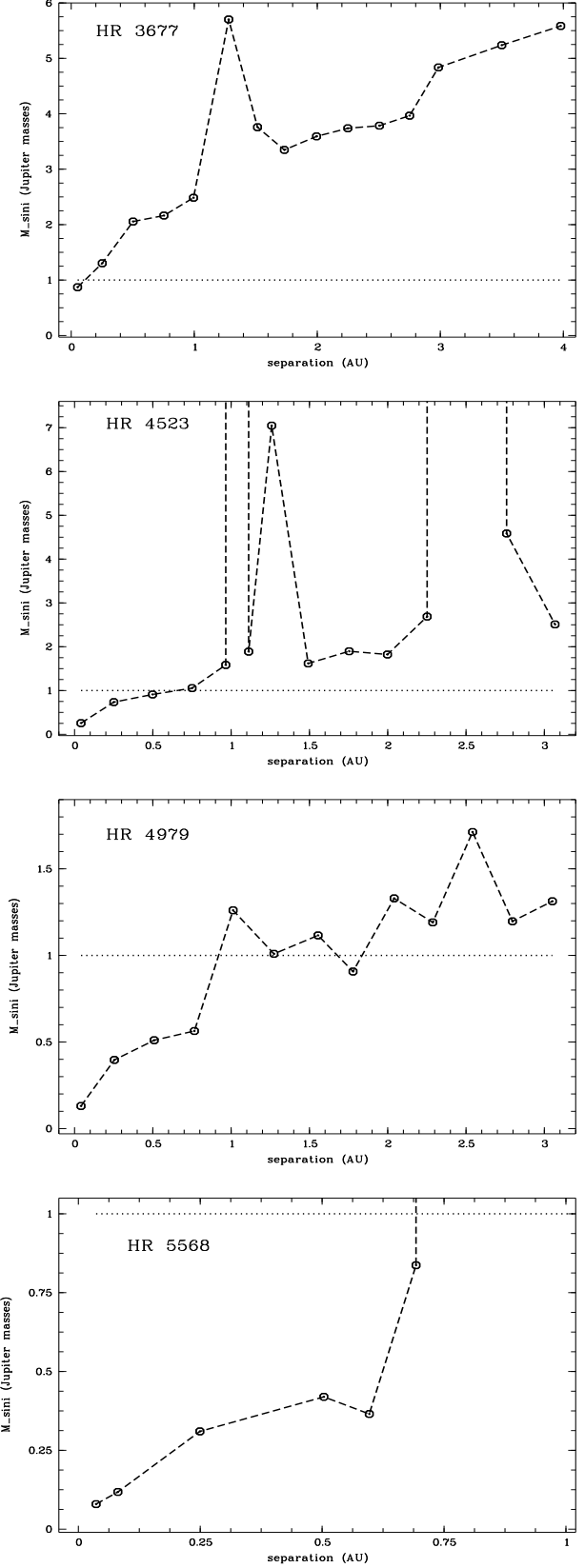


Fig. B.5. Planetary companion limits for HR 3677, HR 4523, HR 4979 and HR 5568.

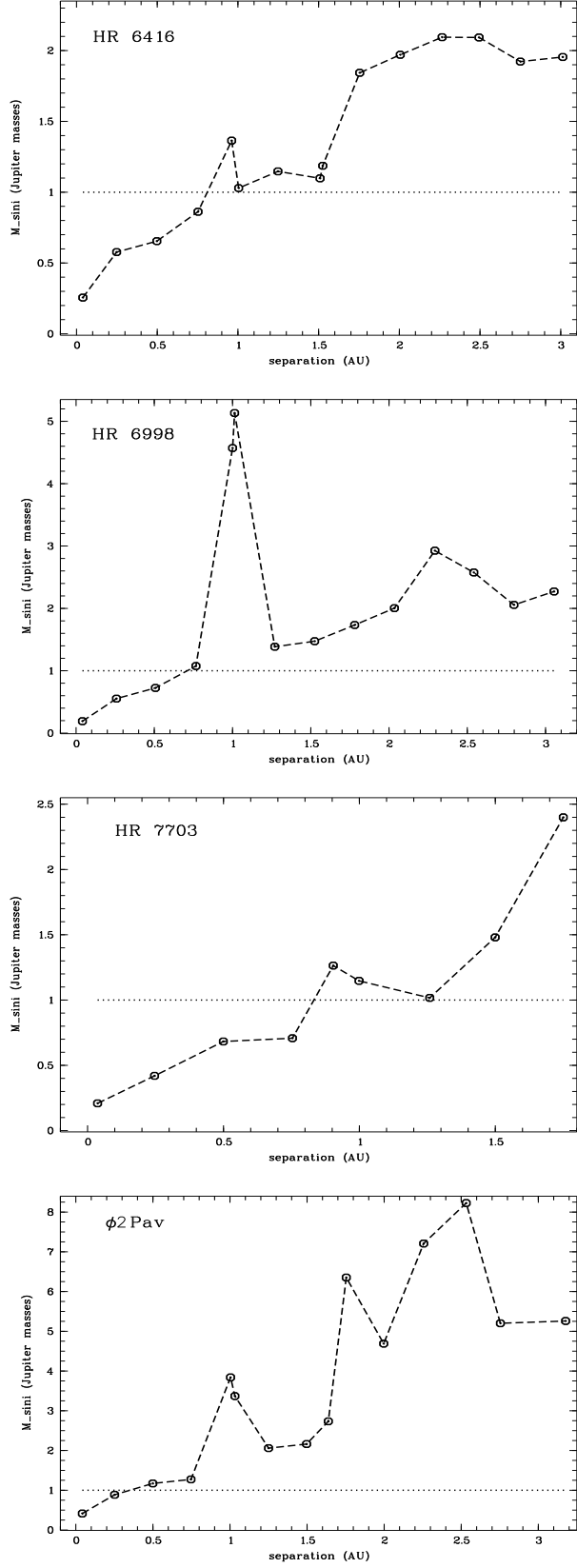


Fig. B.6. Planetary companion limits for HR 6416, HR 6998, HR 7703 and ϕ^2 Pav.

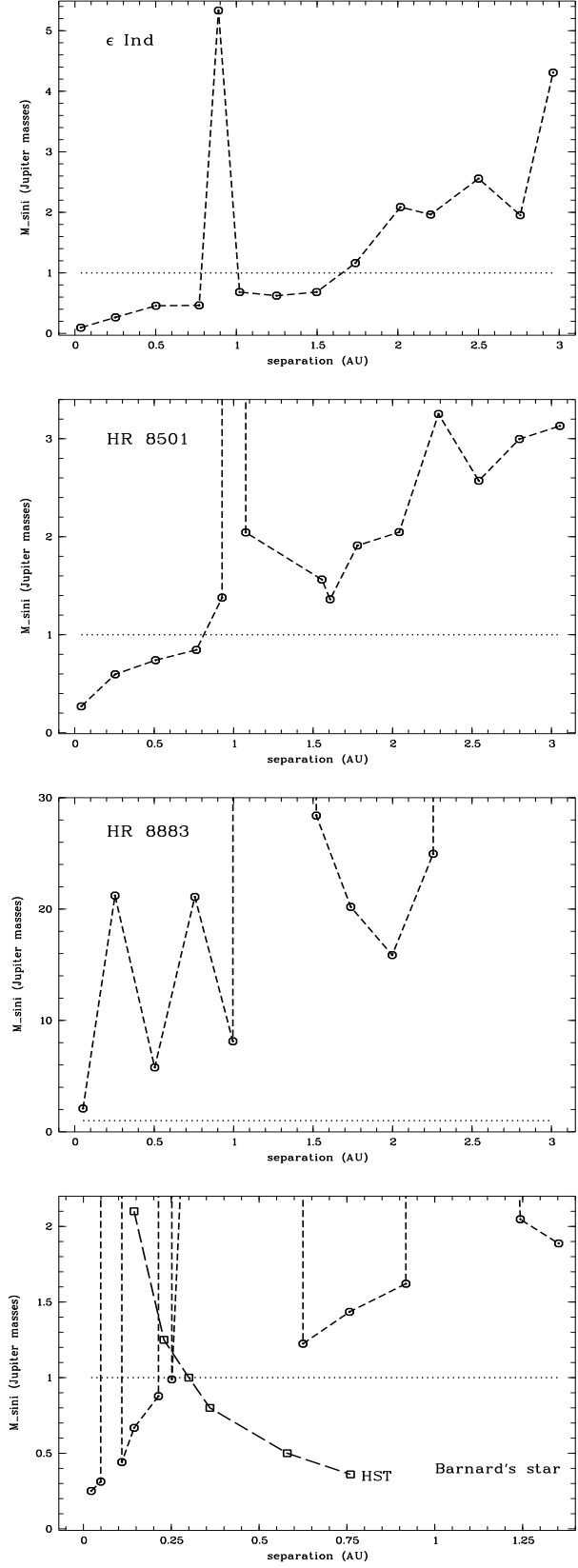


Fig. B.7. Planetary companion limits for ϵ Indi, HR 8501, HR 8883, and Barnard's star.